

Simulation Study on Nonlinear Dynamics of Ballooning Modes in a Spherical Tokamak

Riaz Khan

DOCTOR OF PHILOSOPHY

**Department of Fusion Science, School of Physical Sciences
The Graduate University for Advanced Studies, JAPAN
2006 (School Year)**

Abstract

The ballooning mode is a magnetohydrodynamic (MHD) instability that is excited in finite beta plasmas. The energy source of the ballooning mode originates from the pressure gradient in a locally unfavorable magnetic curvature region, typically, in the outboard of the torus. The proximity of the measured edge pressure gradient in H-mode to the critical gradient for ideal ballooning instability has led to the proposal that these instabilities might have a role in triggering edge localized modes (ELMs). New nonlinear theoretical models describe ELMs in terms of filaments that erupt from the plasma. This is supported by strong experimental evidence from the MAST tokamak[1, 2, 3] that the ELM does indeed exhibit a mode structure predicted by the nonlinear ballooning mode theory. This thesis presents the nonlinear dynamics of the ballooning mode and its relation with ELMs by means of numerical simulations in spherical tokamak (ST) devices in the framework of MHD model and the drift model. Our simulation reproduces the characteristic features of ELM crash phase.

The nonlinear simulations using MHD model are executed in a three dimensional full toroidal geometry. The initial MHD equilibrium for the simulation is given as an axisymmetric numerical MHD equilibrium, which is obtained by solving the Grad-Shafranov equation on the poloidal cross-section. The profiles are selected to be

moderately broad in the core region following the conventional experiments. During the linear analysis, the intermediate- n modes (*i.e.*, $n = 5 - 9$) have larger growth rates than others, where n is the toroidal mode number. It is shown that these intermediate- n modes have a ballooning mode nature in that the mode structures are poloidally localized in the bad curvature region, and have a wide envelope consisting of several poloidal components. In the nonlinear phase, the MHD ballooning modes evolve into a nonlinear structure that results in the formation of a number of hot plasma filaments, elongated along a magnetic field line, but localized about it. These filaments extend out into the scrape-off layer on the outboard side but remain connected back into the pedestal region on the inboard side. This filamentary structure is correspondent to the convection motion of the plasma flows, which forms a twin-vortex flow pattern in such a way that the plasma moves in outward direction, pushing the core plasma from inside to outside of the torus. When the balloon structure is initially formed at the plasma surface, the magnetic field lines on both sides of the separatrix are pushed against each other by such perpendicular flows due to the spouting-out and the perfect conductor conserving the poloidal flux. Under this situation, the reconnection of the field lines can effectively occur by the driven reconnection mechanism. Once such reconnection occur, the plasma rapidly flows out through the reconnected field lines due to the parallel pressure gradient, leading to the filamentary structure. After the internal free energy is partially lost by such convective processes, the system ceases to develop and reaches a relaxed state. These results are compared qualitatively with the experimen-

tal observation of the ELMs in MAST and NSTX experiments. Good agreement is found in the following characteristics formation of filaments separating from the core, non-uniform growth of filaments due to toroidal mode coupling, time scale of ELM crash, triggering by the ideal ballooning mode, presence of intermediate- n precursors and loss of plasma through convective process.

Moreover the finite Larmor radius (FLR) effect is also addressed using the simplified drift model, where the ion diamagnetic drift effect is included in the advection term of the equation of motion. This modification has been found to suppress the higher- n components linearly, since the mode growth is suppressed by the sheared rotation flows. However, it has been also found that the filament separation from the core can take place universally for FLR as well as the MHD case.

Acknowledgments

Many people have taught, encouraged, and supported me throughout my years as a graduate student. I thank them wholeheartedly for their kindness and generosity. Especially, I would like to thank my supervisors late Prof. Takaya Hayashi, Prof. Noriyoshi Nakajima, and Dr. Naoki Mizuguchi in Graduate University for Advanced Studies and National Institute for Fusion Science (NIFS) for their patience, elaborate guidance and continuous encouragement which benefit me a lot throughout my graduate study and will certainly influence me in my future research.

I am grateful to Prof. Yasushi Todo, Prof. Hideaki Miura, Prof. Shoichi Okamura of NIFS and Prof. Kazuaki Hanada of Kyushu University for their useful comments and suggestions.

I express my appreciation to Prof. Hideo Sugama, Prof. Katsuji Ichiguchi, and Prof. Heiji Sanuki of NIFS and Prof. Steve Cowley of UCLA for fruitful discussions. I have learned a lot of things, including the plasma physics and the attitude toward research.

I also wish to thank Dr. Hamid Saleem and the members of Physics Research Division, PINSTECH, Pakistan, for their constant support and encouragement. I am grateful to Dr. Shinsuke Satake, Dr. Masahiro Kobayashi, and Dr. Shigeaki Jimbo of NIFS for helping me through out my student life in Japan.

I would like to thank the secretaries Ms. Mieko Suzuki, Ms Kazuko Mizuno, Ms. Satona Urushihara, and Mr. Atsushi Hibino for all their help. I am profoundly grateful to my parents and my wife for supporting me through many years of study.

Finally I would like to express my deep gratitude to the late Prof. Takaya Hayashi for providing me the opportunity to study the plasma physics in Japan and bring me into the field of plasma simulation. I pray sincerely for the repose of his soul.

This research was funded by the Japanese Ministry of Education, Culture, Sports, Science, and Technology (i.e., Nos. 15760628 and 15540386). Nonlinear simulations were performed on the Sx-7 and Sx-8 Machines at NIFS.

Contents

1 Introduction	1
1.1 Ballooning Modes	2
1.2 Edge Localized Modes	8
1.2.1 Classification of ELMs	10
1.2.2 ELM precursors	14
1.2.3 The importance of the ELM phenomenon	16
1.3 Spherical Tokamak	17
1.4 Experimental observation of MAST	21
1.5 Historical overview of theoretical modeling	25
1.5.1 Ideal MHD	26
1.5.2 Resistive instability	30
1.5.3 Finite Larmor radius correction	31
1.5.4 Nonlinear Ballooning mode theory	34
1.6 Purpose of this study	36
2 Simulation model	38
2.1 Simulation geometry	38

2.2	Physical models	39
2.2.1	MHD model	39
2.2.2	Simplified drift model	42
2.3	Initial equilibrium	44
2.4	Boundary condition	48
2.5	Numerical scheme	49
3	MHD simulation results	52
3.1	Overview of simulation results:	52
3.2	Linear instability	53
3.2.1	Linear growth of instability	53
3.2.2	Linear mode structures	55
3.3	Nonlinear dynamics	59
3.3.1	Formation of filamentary structure	59
3.3.2	Non-uniform growth of filament	62
3.3.3	Field line behavior	62
4	FLR effects	67
4.1	Linear instability	68
4.1.1	Rotation of modes structure	70
4.2	Formation of filamentary structure	74
4.3	Field line behavior	76
5	Discussion	80
5.1	Comparison with observation	80

5.1.1	The mode structure of ELMs	81
5.1.2	The spatial structure of ELMs	84
5.2	Comparison with theory	89
5.3	Effect of FLR correction	90
6	Concluding remarks	93
6.1	Summary	93
6.2	Future directions	95
	Bibliography	97

Chapter 1

Introduction

Nonlinear plasma dynamics, and fast time scale motions in particular, are a recurring theme in both natural and laboratory plasmas. The ballooning mode is a magnetohydrodynamic (MHD) instability that is excited in finite beta plasmas. The energy source of the ballooning mode originates from the pressure gradient in a locally unfavorable magnetic curvature region, typically, in the outer edge region of the tokamak and helical configurations. Nonlinear evolution of such modes results in sporadic releases of plasma heat energy from magnetically confined plasma. Familiar examples of such events are tokamak disruptions and edge localized modes (ELMs). The proximity of the measured edge pressure gradient in H-mode to the critical gradient for ideal ballooning instability has led to the proposal that these instabilities might have a role in triggering ELMs. New nonlinear theoretical models describe both processes in terms of filaments that erupt from the plasma. This is supported by strong experimental evidence from the MAST tokamak [1] that the ELM does indeed exhibit a mode structure predicted by the nonlinear ballooning mode theory. Furthermore, the camera images during shot #8814 of MAST show several helically twisted bright stripes (*i.e.*, filaments) on the plasma surface. Some of them are raised and separated from the core, forming an arcade into the scrape-off layer region. These filaments are generated on a $100\mu\text{sec}$ time scale, are accelerated away from the plasma edge, are extended along the field line and have a typical toroidal

mode number $n \sim 8-10$. This thesis presents the nonlinear dynamics of the ballooning mode and its relation with ELMs by means of numerical simulations in spherical tokamak (ST) devices in the framework of MHD model and the drift model. Our simulation reproduces the characteristic features of ELM crash phase.

1.1 Ballooning Modes

A mode which is localized in regions of unfavorable magnetic field curvature ("bad curvature") and which becomes unstable when the force due to pressure gradients is greater than the mean magnetic pressure force. It was originally described by Coppi [4] and the mathematical formalization was performed by Connor [5].

One of the most important features of the ballooning mode is the effect on stability of the average curvature of the magnetic field. The curvatures of the field lines change sign from the inboard to the outboard side with respect to the curvature of the surfaces of constant kinetic pressure. An understanding of how magnetic curvature affects stability is aided by Fig.1.1. In this plan view of a torus, we can see how on the inboard side, the gradient in magnetic field points in the opposite direction to the gradient in kinetic pressure.

Force balance is given by,

$$F = \frac{B \cdot \nabla B}{\mu_o} - \nabla \left(p + \frac{B^2}{2\mu_o} \right) \quad (1.1)$$

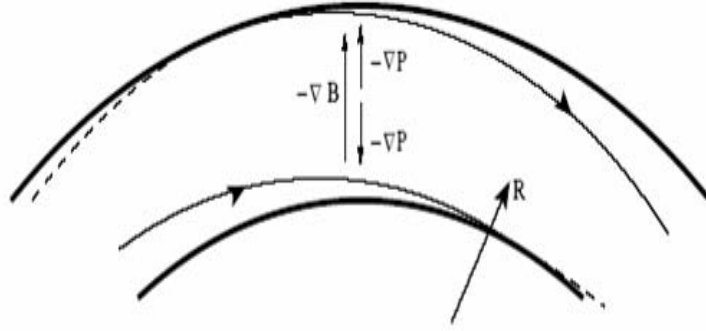


Figure 1.1: Plan view of a section of a torus. The curvature of the \mathbf{B} -field is stabilizing on the inboard side of the torus and destabilizing on the outboard side [8].

Since the majority of the magnetic field is toroidal and falls off as $1/R$, the magnetic tension term, $\mathbf{B} \cdot \nabla \mathbf{B}$ can be simplified to

$$\mathbf{B} \cdot \nabla \mathbf{B} \approx B_\varphi \cdot \nabla B_\varphi = \frac{B_\varphi^2}{R} (-\hat{e}_R) \quad (1.2)$$

where \hat{e}_R is a unit vector in the major radius direction. The magnetic tension force points inward along the major axis on both the outboard and inboard side, whereas the kinetic pressure term $-\nabla p$ points outward on the outboard side and inwards on the inboard side. The force balance is maintained by the magnetic pressure term, $\nabla B^2/2\mu_o$. This asymmetry leads to the phenomena of good and bad magnetic curvature.

Figure 1.2 shows a typical mode structure for a perturbation that destabilizes a ballooning mode. In order to be localized on the unfavorable curvature region, the amplitude variation along the field line must be maximized. Therefore, the most

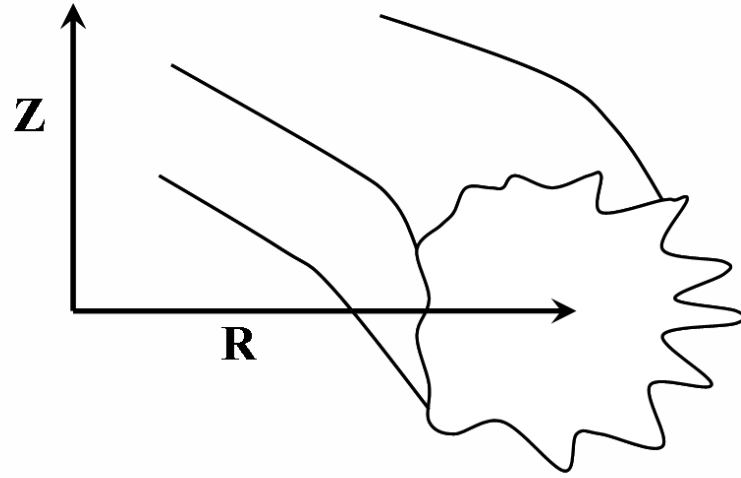


Figure 1.2: The mode structure of ballooning mode. The mode is localized to the unfavourable region of the plasma

unstable ballooning modes typically have high toroidal mode numbers [5]. The mode structure is such that there are very fine structures in the poloidal direction, but in the toroidal direction the wavelength is long. In a tokamak, the toroidal magnetic field is much stronger than the poloidal field. Thus, along the magnetic field line, the mode structure changes slowly, and the stabilizing energy from the field line bending is minimized.

The ballooning mode instability can be further explained by using the energy principle through the change in fluid potential energy associated with the perturbation ξ . This was originally suggested by Furth [6] and Greene [7] and can be written as follows,

$$\delta W_F = \frac{1}{2} \int_{plasma} dr \left[\frac{|\mathbf{B}_{1,\perp}|^2}{\mu_o} + \frac{B_o^2}{\mu_o} |\nabla \cdot \boldsymbol{\xi}_\perp + 2\boldsymbol{\xi}_\perp \cdot \boldsymbol{\kappa}|^2 + \gamma p_o |\nabla \cdot \boldsymbol{\xi}|^2 \right. \quad (1.3)$$

$$\left. - 2(\boldsymbol{\xi}_\perp \cdot \nabla p_o)(\boldsymbol{\kappa} \cdot \boldsymbol{\xi}_\perp^*) - j_\parallel (\boldsymbol{\xi}_\perp^* \times \mathbf{b}) \cdot \mathbf{B}_{1,\perp} \right]$$

where $\mathbf{b} = \mathbf{B}/B$ is the unit vector along magnetic field, $\boldsymbol{\kappa}$ is the curvature vector of the magnetic field $\boldsymbol{\kappa} = \mathbf{b} \cdot \nabla \mathbf{b}$, and $\boldsymbol{\xi}_\perp$ is the component of $\boldsymbol{\xi}$ that is perpendicular to the equilibrium magnetic field. The terms can be interpreted as follows. The $|\mathbf{B}_{1,\perp}|^2$ term is the energy required to bend the magnetic field lines. The second term represents the energy required to compress the magnetic field. The third term is the compressional energy of the plasma. In other words these three term can also be called as the change in potential energy of the Alfvén wave, the magneto-acoustic wave, and the acoustic wave respectively. These three terms are always stabilizing. The last two terms can be either stabilizing or destabilizing. The instabilities caused by the fourth term are called pressure-driven modes, because ∇p is the source of free energy. Typically, ballooning and interchange modes are classified as the pressure-driven types. The last term represents current-driven modes also called as kink mode. Here the source of free energy is the parallel current density j_\parallel . Hence by these five terms as given in (1.3), one can estimate the driving source of the instability.

In determining stability against ballooning modes, the stabilizing field line bending and the destabilizing fourth term of (1.3) (pressure gradient drive) compete with each other. For circular plasmas, this means that the ballooning modes are stabilized by the shear of the magnetic field ($s = r\dot{q}/q$). The stabilizing effect can

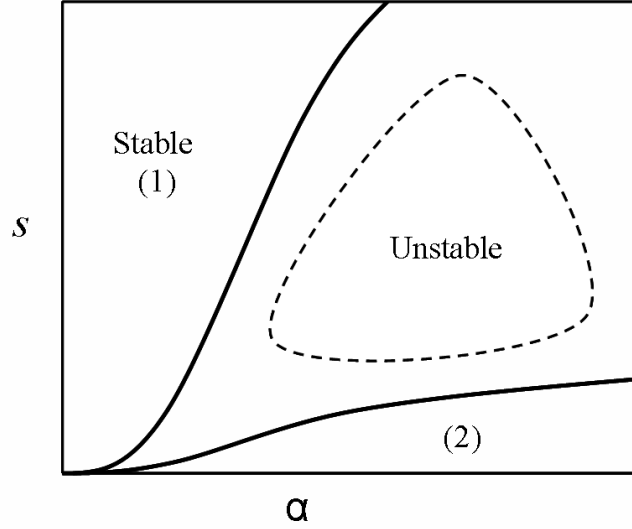


Figure 1.3: Stability diagram of the ballooning mode for circular surfaces showing the first and second stability regions. The quantity $\alpha = -2\mu_o R q^2 p' / B^2$ is a measure of the pressure gradient, and $s = r q' / q$ is the average magnetic shear [8].

be understood by following two magnetic field lines that are only slightly apart in the radial direction. Therefore the mode structure must be almost the same on both field lines. As the field lines are followed around the torus, if there is shear in the magnetic field, the distance between field lines starts growing. This means that in regions of strong shear the mode can not be entirely localized on the unfavorable side and the destabilizing energy is reduced. On the other hand, low shear allows larger radial mode structures to stay together on adjacent field lines. The net effect is that the increasing magnetic shear raises the ballooning stability limit for given pressure gradient.

It turns out that in addition the stable region of high shear and low pressure gradient, there is a second region of stability as well [9]. This stable region has very low shear and high pressure gradient. The reason for this so-called second stable region is the following. What stabilizes the ballooning mode is not actually the global shear, but the local shear in the region where the ballooning mode is localized. This region is the outboard side of the midplane, since there the magnetic shear is most unfavorable. When the global shear is lowered close to zero, the shear on the outboard side becomes negative. The more the local shear varies between the inboard and outboard sides of the flux surface, the more negative the outboard side shear becomes. Since the local shear is determined by the local toroidal current density (the higher the current density, the lower the shear), a large variation of toroidal current density on a flux surface creates also a large variation of the local shear. Also a large pressure gradient creates a large variation of the local shear on a flux surface. Therefore, when the global shear is close to zero, the stability of the plasma against the ballooning modes is improved by increasing the pressure gradient. Unfortunately, the access from the high shear low pressure gradient region to the second stability region for circular plasmas is closed, *i.e.* there is an unstable region between the two stable regions, see Fig. 1.3.

Although for circular plasmas, there is no access from the first stable region (low p' , high s) to the second stable region (high p' , low s), but when the plasma is strongly shaped (increased elongation and triangularity) [10], the stable regions

become connected and the access to the second stable region is opened. The access to the second stable region would make it possible to achieve high pressure values, and to operate the tokamak with high β . The second stability access also plays a role in the edge stability and affects the ELMs.

1.2 Edge Localized Modes

The basic physics of confinement in tokamaks is not well understood. For this reason confinement of particles and energy is modeled by a series of scaling laws which correspond to modes of confinement. When the plasma is externally heated and the temperature gradient becomes steeper, the confinement becomes significantly worse due to the so-called “anomalous” transport. Compared to classical or neoclassical transport, it is usually orders of magnitude faster. The anomalous transport is driven by plasma turbulence. The plasma operating regime where anomalous transport is dominating throughout the plasma is called low confinement mode or L-mode. A great advance in tokamak research was made, when it was discovered that increasing heating of the plasma above a certain threshold improves the confinement considerably [11]. The turbulence then becomes suppressed in the edge region. Since the confinement improvement is not global, the region where turbulence is suppressed is called a transport barrier. The improved confinement operating regime is called high confinement mode or H-mode (see figure 1.4). The key to the success of the H-mode is the edge transport barrier or confinement barrier; a region of steep tem-

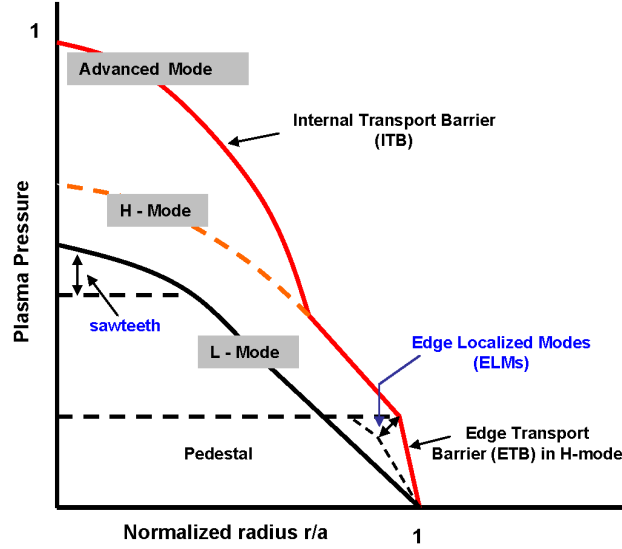


Figure 1.4: Schematic representations of the pressure profiles in L-mode and H-mode (ELMy Hmode). A profile of ELMy H-mode plasma with an internal transport barrier (ITB) is also shown.

perature and density gradient that is formed close to the plasma edge [12]. Figure 1.5 shows electron density profiles over a transition from L-mode. to H-mode on the ASDEX Tokamak [13]. As can be seen, there is a clear increase in the density gradient at the edge of the plasma and a knee is formed in the density profile. The characteristic shape is known as a pedestal and such pedestals have been shown to form during H-modes in both the density and temperature profiles [14].

In H-mode plasmas, short periodic bursts of plasma are often observed. They are called Edge Localized Modes or ELMs[15, 16]. The ELMs are usually detected most easily by the increased radiation coming from the divertor region (the so-called divertor D_α -radiation). The radiation is produced when the particles released from

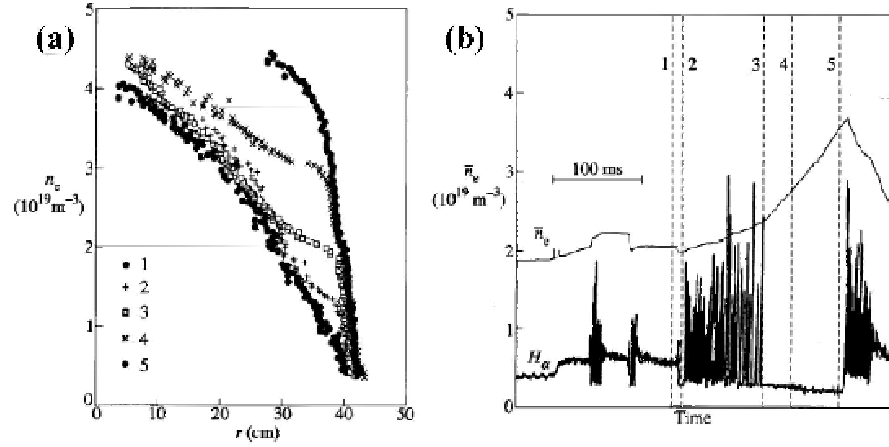


Figure 1.5: The transition from L- to H-mode [13]. (a) Time Sequence of density profiles measured around the transition from L- to H- mode. (b) D_α emission and average density. The dotted lines refer to the times at which the density profiles in (a) were measured.

the edge plasma during the ELM burst collide with neutral atoms that are abundant near the divertor. The collisions excite the atoms and their de-excitation is observed as radiation.

1.2.1 Classification of ELMs

The first classification of ELM phenomena was given for the DIII-D tokamak [18]. Three distinct types of ELM were numbered in the order in which they were discovered.

Type I ELMs

Type I ELMs are large, regular bursts of MHD activity which result in large heat loads to the divertor or limiter plates. The D_α -signal shows large isolated bursts

and, therefore, they are also called 'giant' ELMs. These giant ELMs could well be intolerable in a large tokamak device. They are most easily distinguished because the ELM repetition frequency increases with heating power. They appear at high input power levels, often after a period of ELM-free H-mode. The plasma edge is close to the ideal ballooning stability limit or even beyond it. The time-averaged degradation of the edge plasma confinement is smaller than with other ELM types.

During the onset of such ELMs, pressure gradient in the transport barrier is high, and it is widely believed that they are associated with ideal MHD events. Such ideal MHD instabilities can be divided into two types, the ballooning mode, and the kink (or peeling) mode. As mentioned in previous section the ballooning mode is driven by pressure gradient[19] while the peeling mode are driven by large bootstrap current[17]. Recent studies shows that in certain condition both the pressure gradient and current density are high so that both peeling and ballooning mode stability criteria are violated resulting in the coupled peeling–ballooning mode[17, 20, 21, 22]. In such scenario, if the instability acts to remove the pressure gradient, it further destabilize the peeling mode, leading to a large Type I ELM event.

Type II ELM

Type II ELMs, sometimes called grassy ELMs, are only observed on a few large machines having strongly-shaped (high elongation and triangularity) plasmas like ASDEX-U and DIII-D [11, 18]. Recently big ST like NSTX also observed such ELMs[23]. The magnitude of the ELM bursts is lower and the frequency is higher

than that of Type I ELMs, while the confinement stays almost as good as in Type I ELMy plasmas. It is thought that the increase in triangularity and elongation can give access to a region of so-called second stability [24] to the ballooning mode and it is in this region that type II ELMs are observed [26].

Type III ELM

Type III ELM are the most common, and have been observed on all tokamaks that have achieved H-mode. They are smaller and therefore less damaging than their Type I counter-parts but are still somewhat problematic. Like all ELMs, they lead to a lowering of the edge temperature gradient. Unlike, Type I and type II ELMs, type III ELMs are observed at relatively low input power levels, often prior to a period of ELM-free H-mode[27]. The plasma confinement is degraded more than with other ELMs. The edge plasma pressure can be well below the ballooning stability limit. They are also notably different as their frequency decreases with input power but their magnitude tends to increase. On the ASDEX-U tokamak, type III ELMs are observed below a certain critical temperature $T_e < 300\text{eV}$. This observation suggests that resistivity in the plasma core and therefore the current profile, may play some role in the event. They can also be induced by radiative cooling which cools the edge, increasing its resistivity [21].

ELM-free operating modes

In addition to the above ELMy operating regimes two ELM-free operating modes with stable density have been observed. In DIII-D and ASDEX Upgrade, the so-called quiescent H-mode (QHM) has been achieved [28, 29]. In the quiescent H-mode, the ELMs become suppressed and, instead, harmonic oscillations are observed in the plasma edge. They are signs of other MHD activity that keeps the particle transport high. The high particle transport keeps the density in control and avoids the typical problem of an ELMfree H-mode where the plasma density uncontrollably increases and the discharges ends with a disruption.

In Alcator C-MOD, the so-called enhanced D_α -mode or EDA is observed [30, 31]. In EDA, while the plasma behaves like in ELMy H-mode (steady-state density, no accumulation of impurities), no periodic bursts of plasma exist, but instead the D_α - radiation remains at an increased level throughout the EDA-period. The particle and energy confinement is poorer than in true ELM-free H-mode. The conditions for EDA resemble that of Type II ELMs.

In ASDEX Upgrade, different types of ELMs have been found to correspond to different plasma edge parameters [32]. Figure 1.6 shows schematically the ELM classification in $T_{edge} - n_{edge}$ space. The edge temperature and density refer to the values on the top of the H-mode barrier. The lower limit for the temperature at high density (labelled “MARFE unstable”) is caused by the radiation cooling of the edge plasma and is inaccessible operating regime.

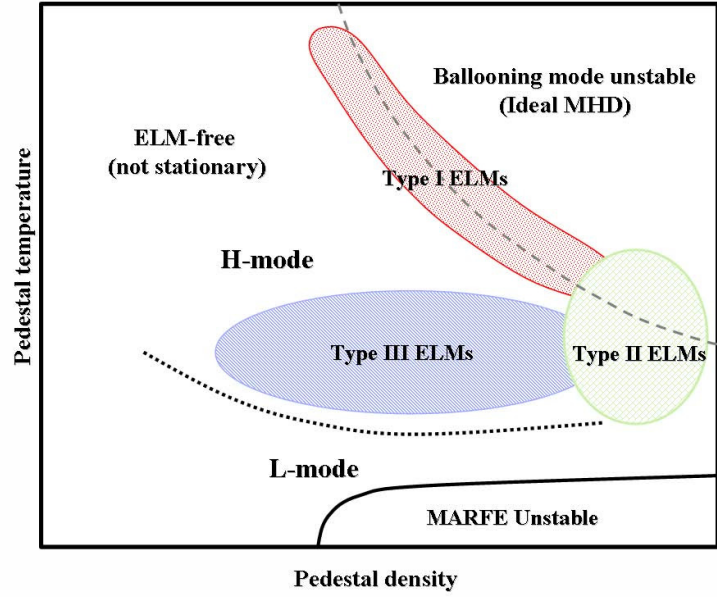


Figure 1.6: A schematic view of different ELMy and ELM-like regimes in the pedestal temperature-density space [8, 32].

1.2.2 ELM precursors

During the ELM cycle, magnetic fluctuations are observed before the main ELM crash. The fluctuations, also called precursors, differ between ELM types, which suggests that the instabilities behind the ELMs themselves can be different. In NSTX, ELMs of several types are often observed: large Type I ELMs, medium Type II/III ELMs and tiny Type V ELMs[23, 33, 34]. Preceding the Type I ELM crash, the Mirnov coil array reveals a rapidly growing precursor having growth time < 100 msec with intermediate mode number $n = 5 - 8$. Preceding the Type II/III ELMs crash, a precursor with frequency $\sim 2\text{kHz}$ and usually mode number $n = 1$ (but occasionally $n = 2 - 3$) appeared for several msec. In case of Type V ELM, a short-

lived $n = 1$ precursor oscillation was observed before the ELM crash, persisting for up to 2 toroidal transits before the crash and disappearing between ELMs.

In ASDEX Upgrade, the precursors are seen most clearly in the Type III ELMs, but they have also been observed with Type I and Type II ELMs. The Type III ELM precursor frequency varies around 50 – 150 kHz and the observed toroidal mode numbers n are of the order 10 – 15 [15, 21]. For type I ELMs frequencies of about 5 – 20 kHz and mode numbers $n = 5 – 10$ are observed. In addition, higher frequency modes (75–145 kHz) with $n = 3–5$ [35] and $\nu \approx 300$ kHz [36] have been associated with the MHD activity occurring before an ELM. The precursors observed with Type II ELM have frequency of about 30 kHz. Typical toroidal mode numbers n are of the order of 3 – 4.

In JET, Type I ELM precursors at the frequency of about 20 kHz and mode numbers of 1 – 13 have been observed [38]. The lower mode numbers seem to be associated with lower values of collisionality in the edge region and high mode numbers with high collisionality. In addition to the precursors, the Type I ELM phenomenon has also been associated with the so-called washboard mode activity (bands of fluctuating magnetic activity rotating in the direction of the electron diamagnetic drift with typical frequencies in the range of 10 – 90 kHz) [39]. The washboard modes have also been observed with mixed Type I/Type II ELMs [39].

While the exact relationship between the precursors and the ELM crash itself is still not clear, the precursors can be used to obtain fundamental information on the

underlying mechanisms for the ELMs. The mode numbers give insight to the mode structure of the instability that is responsible for the ELM. Therefore, to validate a theoretical model for the ELMs, its predictions have to be compared against the information obtained from the precursor observations.

1.2.3 The importance of the ELM phenomenon

The ELMs have a degrading effect on the plasma confinement but, on the other hand, they help to remove impurities and helium ash from the plasma. They also prevent the density of the plasma from rising too high and causing a disruption. Stationary and clean H-mode plasmas without ELMs have been difficult to achieve. Even though in ELMy H-mode it is not possible to keep the confinement as high as in some ELM-free operations, like the hot-ion mode in JET [40], its stable steady state operation and good impurity exhaust in long pulses are superior to other operating regimes. Therefore, ELMy H-mode has been chosen as the standard operating mode for ITER.

Probably the most harmful consequence of the ELMs is the erosion of the divertor plates. From the point of view of the lifetime of the divertor plates, the ELM bursts are much more destructive than the continuous flow of particles and energy. In ITER, the ELM energy may exceed the threshold for divertor target ablation by a factor of 5 [41]. Therefore, reducing the ELM peak power load or getting rid of the ELMs altogether without sacrificing the control of the density and sufficient helium exhaust are important goals that have to be reached on the way to a fusion reactor. In

addition to tokamaks, ELMs have also been observed in stellarator and ST H-mode plasmas [42, 2]. Thus it looks like that the problems associated with the ELMs have to be solved even if one of these alternatives to a tokamak turns out to be better concept for harnessing the fusion energy. It is also interesting to note that solar flares have been found to display similar MHD instability properties as ELMs [43].

1.3 Spherical Tokamak

The name spherical tokamak or Spherical Torus, ST, has been applied to tokamaks with aspect ratio $A = R/a$ (ratio of the major to minor radii of the toroidal plasma column) close to the unity, typically $A < 1.5$. Several important theoretical advantages of this concept with significance for a future fusion reactor were firstly pointed out by Peng and Strickler in 1986 [44]. The success of the START experiment (1991–1998), which demonstrated good confinement [45, 46] and plasma beta values up to 40% [47], led to widespread interest in the ST and the construction of a new generation of much larger STs such as the mega ampere ST (MAST) [48] and NSTX [49]. These devices have poloidal cross-sections and plasma currents comparable to those in major conventional tokamaks such as ASDEX Upgrade and DIII-D. There are thus two main ways in which ST research is helping to advance the mainline tokamak: first, by providing experimental data in new and overlapping parameter regimes to test models and scaling laws (in particular global confinement); and second, by using the fact that the extreme geometry and other special conditions force models to

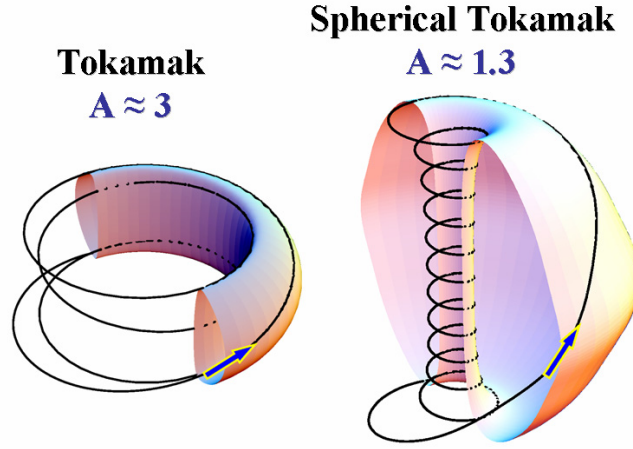


Figure 1.7: Comparison of the conventional (large aspect-ratio) and a spherical (tight aspect-ratio) tokamak plasma configuration (courtesy of Dr. D. A. Gates from NSTX).

be improved or developed. Such models are then available for those conventional aspect ratio tokamak problems where there were known limitations in the existing models.

The transition from high to low aspect ratio is accompanied by the development of a number of properties that have a profound effect on plasma behavior. First and foremost, the low aspect ratio tokamaks could provide a more economical route to magnetic confinement fusion. This was due to their compact size and high core values of $\beta = 8\pi n_o T / B_o^2$ a parameter often employed to express the efficiency of a tokamak. The maximum β that can be obtained in tokamaks is limited by instabilities [50]. This β limit (Troyon limit) is higher in STs due to their low aspect ratio and high elongation [51]. Near the outboard plasma boundary, the poloidal and toroidal

magnetic fields (and hence poloidal and toroidal gyroradii) can become comparable, giving a large field line tilt. The strong toroidicity and increased mirror ratio lead to enhanced trapping and impact on transport, plasma resistivity, etc. High values of β and low aspect ratio also increase the bootstrap current fraction[52]. A model ST power plant is planned to have 92% of its steady-state current drive from a combination of bootstrap and diamagnetic currents [53]. Furthermore, the low moment of inertia of low A plasmas gives rise to high central plasma flow velocities ($v_\phi \sim v_{th}$, where v_{th} is the ion thermal velocity), and there is large inherent $\mathbf{E} \times \mathbf{B}$ flow shear, which has a strong influence on micro-turbulence and the formation of transport barriers. As a result of the low magnetic field, supra-Alfvénic ions are readily generated, leading to the excitation of fast particle driven instabilities such as Alfvén eigen modes.

In a conventional tokamak, plasma current is driven inductively from a central solenoid, and initially the plasma is heated Ohmically ($P = I^2 R$). STs have a narrow centre column, consequently there is very little space for a solenoid, and so inductive current drive and Ohmic heating are limited. An important problem at ST is the thermal load on plasma facing surfaces, which would be distributed over a smaller area than in a conventional tokamak. In addition, due to the small inboard space, neutron shielding of the centre column would be thinner in a ST reactor, and would then require more frequent replacement. The lack of access would provide an engineering challenge for remote handling of activated surfaces, greater than that currently

demonstrated in JET. STs are more resilient to large scale MHD instabilities (disruptions). The strong variation of $|\mathbf{B}|$ on a flux-surface in STs causes particles to spend more time on the good-curvature side of the tokamak, increasing the stability of ballooning-like modes. However, the same magnetic field profile causes a larger fraction of particles to be trapped in the bad curvature region, especially on the outer flux surfaces.

The ST concept has been experimentally investigated in several small devices such as START, PEGASUS, MEDUSA [8] and the promising results (record $\beta_t \sim 40\%$, resilience to disruptions, comparable energy confinement time to conventional tokamaks, etc. [47, 54]) have engendered a worldwide next generation programme of large tight aspect ratio experiments (MAST, NSTX, GLOBUS-M, ETE, TST). The excellent diagnostic visibility afforded by the spherical geometry of the MAST tokamak, remote first wall and extensive divertor and edge diagnostics make it an ideal device for the study of ELMs. Especially the unique capability of imaging the whole MAST plasma allows scientists to view how the plasma interacts with the coils and wall of the machine when it gets out of control and “disrupts”. It motivated us to investigate the ELM characteristic and extract information from the experimental observation of MAST. Table 1.1 show the values of engineering, heating and plasma parameters for the famous ST experiment. These devices will serve to improve understanding of the physics of toroidal plasma systems, extending the parameters of

		START	MAST	NSTX
Major Radii	R [m]	0.35	0.85	0.85
Minor Radii	a [m]	0.27	0.65	0.68
Elongation	κ	1.5 – 3	≥ 2 (2.45)	2.7
Aspect Ratio	A	1.29	≥ 1.3 (1.3)	1.27
Plasma current	I_p [MA]	0.31	2 (1.35)	1.0 (1.5)
Toroidal field	$B\phi$ [T]	0.2 – 0.6	0.52	0.3 – 0.6
Auxiliary heating	P_{NBI} [MW]	1 <i>NBI</i>	5 (3.3) <i>NBI</i>	5 (7) <i>NBI</i>
	P_{RF} [MW]	0.2 <i>ECH</i>	1.4 (0.9) <i>ECH</i>	6 (4) <i>FW</i>
Normalized pressures	β_N	6	5.3	7.5
	β_t %	40	17	39
Pulse length	τ_p [s]	0.05	5 (0.7)	5 (> 1)

Table 1.1: Comparison of the key operational parameters of START, MAST and NSTX. Figures in the brackets indicate values achieved [55, 56].

spherical devices to larger, hotter and collisionless regimes as well as develop scalings for aspect-ratio and linear dimensions.

1.4 Experimental observation of MAST

The Mega Amp Spherical Tokamak (MAST) at UKAEA Fusion is a second generation ST designed to study low collisionality, low aspect ratio (ratio of major radius R to minor radius a of $A \sim 1.3$), highly elongated ($\kappa > 2$) plasmas with a plasma current and poloidal cross-section comparable to medium sized conventional tokamaks such as DIII-D and ASDEX-Upgrade. The toroidal field varies between $1.7T$ at the inboard mid-plane and $0.25T$ at the outboard. This strong variation across the plasma is a distinct feature of the ST. Experiments on the MAST are focused on the core goals of improving fundamental understanding of transport, stability and edge physics and investigating technological solutions to heating, current drive and plasma

exhaust, both for ITER and future ST devices. This section presents an overview of recent experimental results, and analysis on MAST related with edge physics especially ELMs.

ELMs are a concern for ITER as they could lead to damage to plasma-facing surfaces. Improved understanding of ELMs is necessary to calculate their effect on power loading, both on the first wall and divertor target plates. MAST plasmas exhibit a number of advantageous features for the study of ELMs structure especially in explaining the spatial localization of ELM structure. The remote first wall and excellent access for imaging diagnostics, combined with the low magnetic field and large field line pitch angle at the outboard mid-plane facilitate diagnosis of ELM characteristics that is simply not possible on most other devices[1, 2]. The overwhelming evidence for the filamentary structure of ELMs comes from unique visible imaging capabilities, the clarity of images being substantially enhanced by the large field line pitch angle. Such images are supported by detailed Langmuir probe and plasma rotation measurements which show that the ELMs are associated with a filamentary structure of toroidal mode number typically $n \sim 10$, rotating with a toroidal velocity of $\sim 15 \text{ km s}^{-1}$ [3]. Figure 1.8 shows the evidence of filamentary structure at the start of ELM. As the ELM develops further, the filamentary structure pushes out into the SOL and provides a conduit for a rapid particle and energy losses from the pedestal region. Similar filamentary structure were also obtained in COMPASS-D indirectly from magnetic measurements [63].

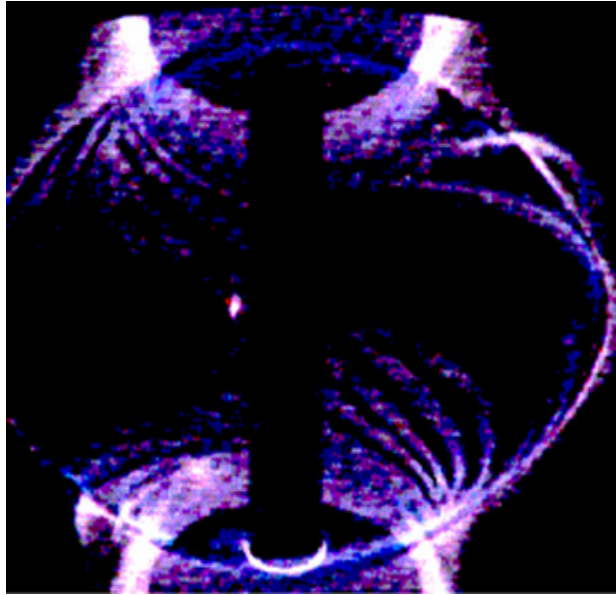


Figure 1.8: High speed visible image of the MAST plasma (#8814) at the start of an ELM, showing evidence for a filamentary structure that follows the field line near the plasma boundary[1].

The capability of the Thomson scattering systems to monitor both inboard and outboard pedestals has shown the formation of broad tail in both the density and temperature profiles at the outboard midplane but no change on the inboard side, showing that the ELMs in MAST have a ‘ballooning’ character and are convective in nature, affecting primarily the outboard pedestal density profile. A sequence of pedestal density profiles is illustrated in figure 1.9 showing the formation of steep gradient in density and temperature profile in pedestal region just before the onset of ELM, later during the onset of ELM, broadening of the profile occurs as shown in Fig. 1.9(b). At this time, narrow plasma filaments develop, locally perturbing the outboard separatrix and flux surfaces in SOL region as shown in Fig. 1.9(e). Finally

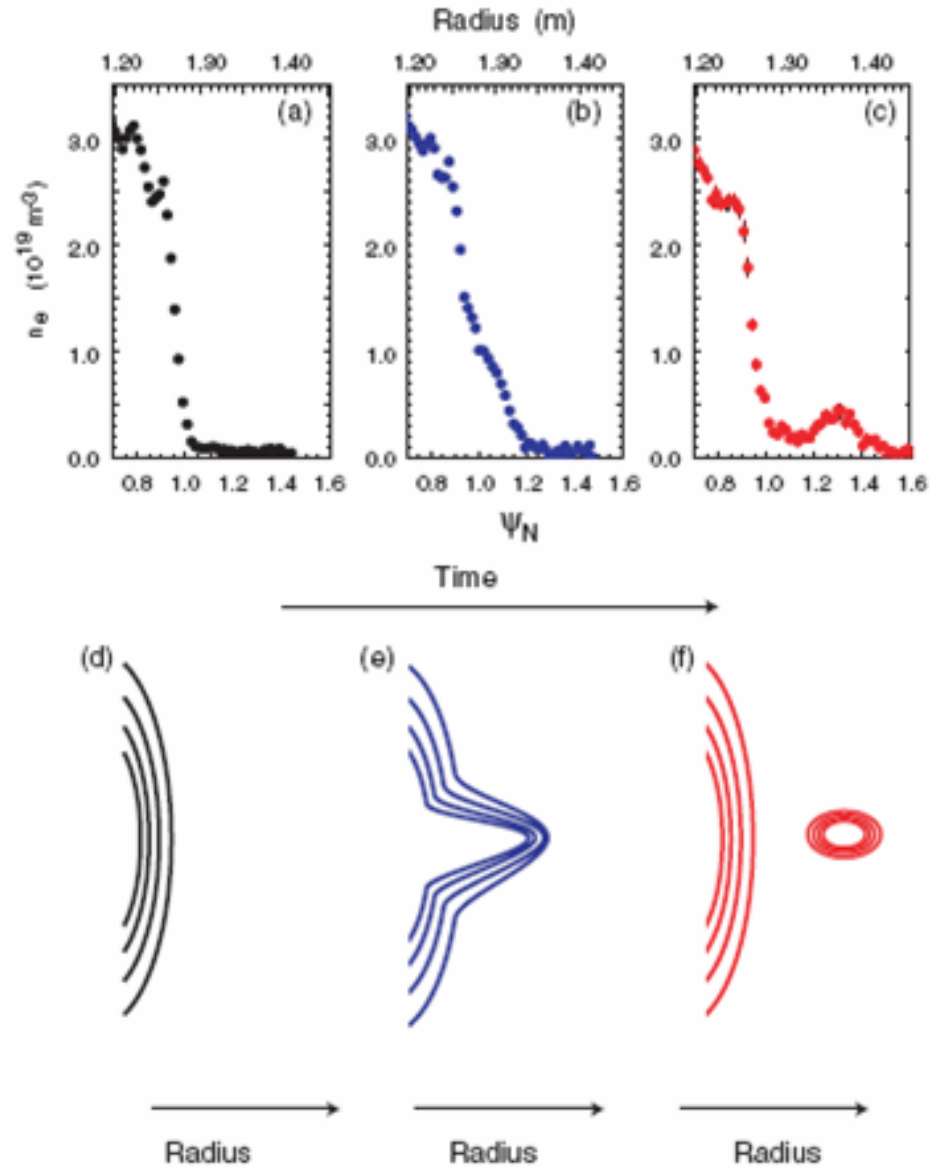


Figure 1.9: Thomson scattering profiles of the outboard edge density profile in normalized flux coordinates at different times with respect to the start of a similar ELM, (a) shot 5752 before the ELM, (b) shot 5756 in the middle of the ELM rise, and (c) shot 5864 near the end of the ELM rise time [3].

the ‘detachment’ of the plasma filament at outboard midplane is shown in 1.9(c and f) [3]. Similar behavior is seen in measurements from detailed studies enabled by MAST’s unique imaging capabilities, have shown how plasma filaments form and disturb the edge of the plasma. This disturbance to the outboard flux surfaces leads to enhanced cross-field transport of heat and particles from the filament into the scrape-off layer, beyond the separatrix. Since the filament is linked to the core it acts as a conduit for losses from the whole pedestal region *i.e.* much more energy would be lost during the process than there is contained, at any one time in the filament volume. Finally, by magnetic reconnection, the filament detaches from the core at the outboard mid-plane [2, 3]. The above interpretation of the formation and detachment of filamentary structure are based on the nonlinear ballooning mode theory of Wilson and Cowley [64] and will be explained in detail in later section.

1.5 Historical overview of theoretical modeling

MHD theory provides a single fluid description of long wavelength, low-frequency, macroscopic plasma behavior. The governing equations for MHD theories are Maxwell’s equations, mass, momentum and energy conservation equations and ohm’s law. When we take $\eta \rightarrow 0$, such a model is called ‘ideal’ MHD theory, where the plasma is considered to be perfectly conducting in contrast when $\eta \neq 0$, it is called ‘resistive’ MHD theory. In general, kinetic effects are not considered in conventional MHD theory not only because they complicate the procedures of analysis but also because most of the

important macroscopic MHD phenomena have been successfully described without including the kinetic effects in the past.

1.5.1 Ideal MHD

Ideal MHD theory has been reviewed excellently by Freidberg[66], and readers are referred to his book for a more detailed discussion. For ideal MHD theory, the governing equations are derived from the Maxwell-Boltzmann equation;

$$\frac{\partial f_j}{\partial t} + \mathbf{u} \cdot \nabla_r f_j + \frac{q_j}{m_j} (E + \mathbf{u} \times \mathbf{B}) \cdot \nabla_u f_j = \left(\frac{\partial f_j}{\partial t} \right)_c \quad (1.4)$$

Here $f_j \equiv f_j(x, \mathbf{v}, t)$ is a distribution function for species j . Braginskii [67] showed complete derivation for fluid moments of species j from the general kinetic model. After deriving mass, momentum and energy conservation equations for electron and ion species, we may obtain a single fluid model from the two-fluid equations. Assuming no dissipation ($\nu = 0$) and isotropic plasma, the ideal MHD model can be described as a single fluid in the following equations ;

continuity equation

$$\frac{\partial \rho}{\partial t} + \nabla \cdot \rho \mathbf{v} = 0 \quad (1.5)$$

equation of motion

$$\frac{\partial}{\partial t} (\rho \mathbf{v}) + \mathbf{v} (\nabla \cdot \rho \mathbf{v}) + \rho (\mathbf{v} \cdot \nabla \mathbf{v}) = \mathbf{j} \times \mathbf{B} - \nabla p \quad (1.6)$$

equation of state

$$\frac{\partial p}{\partial t} + \nabla \cdot (p\mathbf{v}) + (\gamma - 1)(p\nabla \cdot \mathbf{v}) = 0 \quad (1.7)$$

Ohm's law

$$\mathbf{E} + \mathbf{v} \times \mathbf{B} = 0 \quad (1.8)$$

Faradays's law

$$\frac{\partial \mathbf{B}}{\partial t} = -\nabla \times \mathbf{E} \quad (1.9)$$

Ampere's law

$$\nabla \times \mathbf{B} = \mu_o \mathbf{j} \quad (1.10)$$

$$\nabla \cdot \mathbf{B} = 0 \quad (1.11)$$

A characteristic dimension for MHD phenomena is the overall dimension of the plasma, denoted by L also called characteristic MHD length. The typical characteristic time scale of ideal MHD is set by the thermal velocity of the ions, *i.e.* $\mathbf{v}_{th} = (2T_i/m_i)^{1/2}$. This is the fastest velocity at which the plasma as a whole can be moved. Also the MHD ordering in terms of characteristic MHD frequency ω and wavenumber denoted by k can be written as follows:

$$\begin{aligned}\omega &\sim \frac{\partial}{\partial t} \sim \frac{\mathbf{v}_{th}}{L} \\ k &\sim \nabla \sim \frac{1}{L}\end{aligned}\tag{1.12}$$

and similarly, the resulting velocity

$$\frac{\omega}{k} \sim v \sim \mathbf{v}_{th}$$

In the MHD theory, it is essential that the plasma is collisional, *i.e.* the particles interact frequently with each other. Without this assumption such quantities as temperature or pressure of the fluid element can not be defined. On the other hand, if ideal MHD is considered, plasma should not be too collisional, since it is assumed that the resistivity of the plasma is small. Low resistivity allows to neglect such phenomena as resistive diffusion and reconnection of magnetic field lines.

The following are the condition of validity of ideal MHD which must be satisfied [66]:

1. The collisionality must be large in order to keep ion and electron temperatures equal and to ignore the viscous effects.
2. The ion gyro radius must be small compared with the characteristic length scale of the MHD phenomena.
3. The resistivity must be small to avoid resistive diffusion.

The second and the third condition are satisfied for most plasmas that are interesting from the fusion point of view. Unfortunately, the first condition is not. The col-

lisionality is too low for the particle motion parallel to the magnetic field lines to be treated accurately by ideal MHD. However, since the charged particles gyrate around magnetic field lines, they can be assumed to be “frozen” to the field lines. This means that, while the particle motion is very rapid in the parallel direction, gyro-averaged perpendicular particle motion is slow and, consequently, the collisional effects are fast compared with the transport across the field lines, so that the perpendicular behavior can be treated with the fluid model. This allows treating most fusion plasmas with the ideal MHD theory in the direction perpendicular to the magnetic field. Fortunately, in toroidal devices, like the tokamak, this has little effect on the equilibrium and stability of the plasma. Consequently, the ideal MHD model for tokamak fusion plasmas can be used in most cases.

It is also good to keep in mind the limitations of the MHD theory. For instance, if the particle orbit radius is comparable to the gradient lengths of the plasmas, averaging the particle position over the Larmor orbit is no longer justified and even the perpendicular MHD has reached its limit of validity. For instance, in the region near the tokamak plasma edge, where a steep pressure gradient exists, MHD theory is close to the limit of validity and some effects caused by the finite ion gyro radius start to play a role in the MHD stability of the plasma.

1.5.2 Resistive instability

In the preceding section we discussed plasmas with zero resistivity. In such a case conducting plasma is frozen to the line of magnetic force. However the resistivity of plasma is not generally zero and the plasma may deviate from the line of magnetic force. Modes which are unstable in ideal case may in some instance become unstable if finite resistivity is introduced. Hence considering a finite resistivity $\eta \neq 0$ in Ohm's law 1.8, the ideal MHD equations may be modified for resistive stability studies.

$$\mathbf{E} + \mathbf{v} \times \mathbf{B} = \eta \mathbf{j} \quad (1.13)$$

Hence, the perturbed linearized Ohm's law becomes

$$\begin{aligned} \frac{\partial \mathbf{B}_1}{\partial t} &= \nabla \times (\mathbf{v}_1 \times \mathbf{B}_0) - \nabla \times \left(\frac{\eta}{\mu_o} \nabla \times \mathbf{B}_1 \right) \\ &= \nabla \times (\mathbf{v}_1 \times \mathbf{B}_0) + \frac{\eta}{\mu_o} \nabla^2 \mathbf{B}_1 \end{aligned} \quad (1.14)$$

The second term of the RHS of (1.14) contains the finite resistivity of the plasma and allows us to investigate the resistive instabilities. From a physical point of view, it represents the diffusion of magnetic field lines through plasma and its characteristic time is the so-called 'resistive diffusion time', $\tau_R (\equiv \mu_o L^2 / \eta)$. The shortest characteristic time in the plasma is of the order of the Alfvén time, $\tau_A \equiv L / v_A$, where $v_A = B_o / \sqrt{\mu_o \rho}$, while the longest time is of the order of τ_R . Thus, the Lundquist Number (or magnetic Reynolds number) $S_0 (\equiv \tau_R / \tau_A)$ is used for characterizing the plasma. For typical tokamak plasmas, S_0 is on the order of 10^6 to 10^8 , so the re-

sistive diffusion time and the Alfvén time are well separated. As a rule of thumb, a typical MHD characteristic time is on the order of the geometric mean of τ_R and τ_A and an ideal MHD characteristic time is faster than that of resistive MHD. To distinguish the resistive instabilities from ideal MHD, the MHD modes are called resistive ballooning, resistive interchange, resistive kink, and tearing modes etc.

1.5.3 Finite Larmor radius correction

Ideal MHD instabilities play an important role in limiting plasma performance in tokamaks. Its effect on plasma confinement becomes even more important if the MHD modes are associated with the so-called transport barriers (*i.e.* large pressure gradient region), which suppress the thermal plasma transport in a narrow region and control high confinement of the plasma. In such high pressure gradient region, one must take into account all the relevant pressure-dependent effects, which can modify the stability conditions. One of the well-known effects, which can dramatically modify the stability of ideal MHD modes is the finite gyroradius effect of the ion diamagnetic drift frequency ω_{*i} , which can stabilize ideal MHD modes if their growth rate γ_{MHD} is comparable to or lower than ω_{*i} [68, 69, 70]. Such effects can be introduced through the drift ordering, by addition of few terms in the ideal MHD equations. The modified MHD model is also called as drift model.

As mention in the earlier section (*i.e.* 1.5.1), the MHD ordering is based on ion thermal velocity scales $v \sim v_{th}$ and $\omega \sim v_{th}/L$. However the drift ordering [71] brings the velocity and growth rate scales one order smaller,

$$v \sim \delta v_{th}, \quad \frac{\partial}{\partial t} \sim \delta \frac{v_{th}}{L}, \quad \frac{\omega}{\Omega_{ci}} \sim \delta \frac{\rho_i}{L} \sim \delta^2 \quad (1.15)$$

where δ is the characteristic small parameter, Ω_{ci} is the ion cyclotron frequency and ρ_i is the ion gyroradius. The drift model avoid trivial complications by assuming equal species temperature, $T_i = T_e$. The quasineutrality condition makes both pressure the same, (*i.e.*, $p_i = p_e$) with the total pressure becomes $p = p_i + p_e$. The fluid velocity can be written as

$$\mathbf{v}_i = \mathbf{v} + \mathbf{v}_{dia} \quad (1.16)$$

and

$$\mathbf{v} = \mathbf{v}_\perp + \mathbf{v}_\parallel \quad (1.17)$$

corresponds to MHD velocity in the limit of vanishing gyroradius. The drift ordering introduces the diamagnetic velocity as \mathbf{v}_{dia}

$$\mathbf{v}_{dia} = \frac{\mathbf{B} \times \nabla p}{qnB^2} \quad (1.18)$$

where q is the particle charge. Using the above definition we can write two forms of drift model equation, the first model is called as Hazeltine drift model (HZ)[71]

$$\frac{\partial n}{\partial t} + n \nabla \cdot \mathbf{v}_i = 0 \quad (1.19)$$

$$m_i n \left(\frac{\partial \mathbf{v}}{\partial t} + \mathbf{v} \cdot \nabla \mathbf{v} + \mathbf{v}_{dia} \cdot \nabla \mathbf{v}_\perp \right) = \frac{1}{c} \mathbf{j} \times \mathbf{B} - \nabla p \quad (1.20)$$

$$\mathbf{E} + \mathbf{v}_i \times \mathbf{B} + \frac{1}{2en} (\nabla p - 2\mathbf{j} \times \mathbf{B}) = \eta \left(\mathbf{j} - \frac{3cn}{4B} b \times \frac{\nabla p}{n} \right) \quad (1.21)$$

$$\frac{dp}{dt} + \frac{5}{3} (p \nabla \cdot \mathbf{v}) = 0 \quad (1.22)$$

However in Chang and Callen model (CC)[72], they uses the total ion fluid velocity \mathbf{v}_i , and retain a partial derivative of \mathbf{v}_{dia} , that was neglected in (1.20), and hence we can write the equation of motion of Chang and Callen model as

$$m_i n \left(\frac{\partial \mathbf{v}_i}{\partial t} + \mathbf{v}_i \cdot \nabla \mathbf{v}_i - \mathbf{v}_{dia} \cdot \nabla \mathbf{v}_i \right) = \mathbf{j} \times \mathbf{B} - \nabla p - \nabla \cdot \Pi_i^{gv} + \mu \nabla_\perp^2 \mathbf{v}_i \quad (1.23)$$

, if we compare CC equation of motion and HZ equation of motion, ones sees the parallel gyroviscous force term (*i.e.*, $\nabla \cdot \Pi_i^{gv}$). This term algebraically cancel a significant part of the advective acceleration $n \mathbf{v}_i \cdot \nabla \mathbf{v}_i$. This is also called as gyroviscous cancellation[72], and is written as follows

$$n \left(\frac{\partial \mathbf{v}_{dia}}{\partial t} + \mathbf{v}_i \cdot \nabla \mathbf{v}_{dia} \right) + \nabla \cdot \Pi_i^{gv} = \nabla \chi - \mathbf{b} n (\mathbf{v}_{dia} \cdot \nabla \mathbf{v}_\parallel) \quad (1.24)$$

where $\chi = -p_i b \cdot (\nabla \times \mathbf{v}_\perp)$ is a scalar related to parallel component of ion vorticity.

The main difference between these equations and the equation of MHD model is through slight modification to the scalar pressure and the appearance of source term proportional to \mathbf{v}_{dia} . Thus the drift model naturally produces the set of equations that explicitly contain the lowest order finite Larmor radius correction to the MHD model. This has been proven to be powerful tool for analysis of hot, well confined plasma such as tokamak.

1.5.4 Nonlinear Ballooning mode theory

The theory for the early nonlinear evolution of ballooning modes in geometry of a tokamak was developed by Cowley and Wilson [43, 64, 65]. This study was done by keeping astrophysical application in mind. The field lines were assumed to be held fixed at the two end points. Such a boundary condition are applicable to the plasma edge where at certain rational surface the field lines connect back on themselves after a finite number of revolutions around the torus. A number of approximation were taken inorder to limit it to the early nonlinear phase. First, the perturbation has a long wavelength in the direction along the magnetic field lines and is described by the standard linear ideal MHD ballooning mode equation at marginal stability[75]. The nonlinearity enter the equation for the variation of the perturbation perpendicular to the field line, which is time-dependent. The perturbation is defined as

$$\xi(\psi, \alpha, \theta; t) = F(\psi, \alpha; t) H(\theta) \quad (1.25)$$

where H is the solution to the ballooning equation at marginal stability, the nonlinear equation that determines F is

$$\begin{aligned} \frac{\partial^2}{\partial t^2} \frac{\partial^2}{\partial \alpha^2} \left[\int_0^t dt \frac{u(\alpha, \psi; t)}{(t - t^*)^{\lambda-1}} \right] = & \left[2(1 - \mu) \frac{\partial^2 u}{\partial \alpha^2} - C_1 \frac{\partial^2 u}{\partial \psi^2} \right] + C_2 \frac{\partial u}{\partial \alpha} \left[\left(\frac{\partial u}{\partial \alpha} \right)^2 \right] \\ & + C_3 \frac{\partial^2 u}{\partial \alpha^2} \frac{\partial^2}{\partial \psi^2} \left(\overline{\frac{\partial u}{\partial \alpha}} \right)^2 \end{aligned} \quad (1.26)$$

The first two terms on the right-hand side are standard linear terms. The first term represents the linear drive for the unstable flux tube and close to linear marginal stability is positive (unstable) in a narrow region of ψ . The second represents the stabilizing terms that come from pushing aside flux tubes to allow the exploding tube through. For small amplitude the displacement is confined to the narrow linearly unstable region. The third term that is quadratic in u is the nonlinear drive due to the weakening of the stabilizing field line bending as the flux tube expands. This gives rise to an explosive evolution of the instability and a narrowing of the mode in the poloidal direction. An additional third order term resulting from the evolution of the pressure gradient leads to a widening in the radial direction as the local pressure gradient at the centre of the mode is moved outwards by the instability. The resulting picture is that of a localized flux tube being expelled from the main plasma in an explosive manner. This flux tube is connected back to the plasma. This model can explain the filamentary structures observed in MAST to some extent, however it didn't address the loss mechanism of energy.

1.6 Purpose of this study

The main purpose of this study is to investigate the nonlinear dynamics of the ballooning mode by means of numerical simulations in ST devices in the framework of MHD model and the drift model. One of the example of time evolution of nonlinear ballooning mode instability is the ELMs. In the current work, we aim to explain the scenario of an ELM crash with a spontaneous time development of plasma from the beginning to the end continuously and self-consistently. This should be placed upon the first attempt to understand the eruption of filamentary structure from the edge pedestal during ELM crash. This study will help to close the gap between the experimental observation and theoretical modeling, and will reveals new informations that will be helpful to improve the current understanding of the spatial and temporal structure of ELMs.

Bearing in mind the above objective, most of this study is devoted to reproduce the eruption mechanism of filamentary structure by the simulation. Since the mechanism of filaments is not understood at all, we firstly aim to understand the outline of the phenomenon by using as simple model as possible. Thus, we carry out MHD simulation in a three-dimensional full toroidal geometry to investigate the characteristic feature of ELM burst which is considered to be governed by large scale activities. The simulation results are immediately compared with the experimental results, and the discrepancy between them are fed back to the modeling. Repeating

such investigations many times, we can improve the modeling and can reproduce the phenomenon appropriately.

Experimentally, the filamentary structures associated with ELMs has been already observed in multiple tokamaks (*i.e.*, MAST, NSTX and ASDEX-U). These filamentary structure have the following characteristic features: localized structure along the field line, occurrence during the H-mode of operation, occurrence near ballooning stability limit, convective loss of plasma, rapid growth of intermediate precursor preceding the crash, ELM rise time $\sim 100\mu\text{sec}$. Hence our target is to reproduce the above characteristic features of ELMs through simulation. Moreover in the second part of our simulation, we will introduce a diamagnetic rotation of the perturbations in both toroidal and poloidal directions. These rotations will be introduced in the MHD momentum equation through the advection term due to the ion diamagnetic drift effect. This will improve our simulation model, and the simulation results will become more realistic and comparable with the experimental observation.

In the following chapter, the simulation models are described, with the detail regarding the initial equilibrium, the boundary conditions, and the numerical schemes. In chapter 3 and 4, the simulation results using the MHD model as well as the drift model are presented. Chapter 5 shows the comparison between simulation result and the experimental observation by using MHD and FLR models. And finally, the summary of this study and some remarks are described in the last chapter.

Chapter 2

Simulation model

2.1 Simulation geometry

The principal aim of our simulation is to understand the nonlinear dynamics of ballooning modes and explore the formation of ballooning filaments which erupts during ELMs in high beta plasma. Our simulations are based on standard resistive MHD model. These simulations are executed in a three dimensional full-toroidal cylindrical (r, θ, z) geometry as shown in Fig. 2.1, where r is the major radial coordinate, θ is the toroidal angle and z is the vertical distance along the axis of the ST. The poloidal cross-section is clipped in rectangular shape, including the external open magnetic field. The external region is simply modelled by filling a uniform low-pressure plasma initially to improve the numerical instabilities. The boundary condition is periodic in toroidal direction, and the perfect-conducting no-slip wall at all the physical boundaries. The region where simulation is performed includes both the core plasma and the peripheral magnetic field. The plasma can freely extend into the peripheral region as a result of time development. A conductor rod is placed on the center of the cylinder. Since the plasma motion that is propagated by the Alfvén wave is disturbed at the top and the bottom boundary, therefore the simulation result is more sensitive to the conditions of these boundaries than the inner

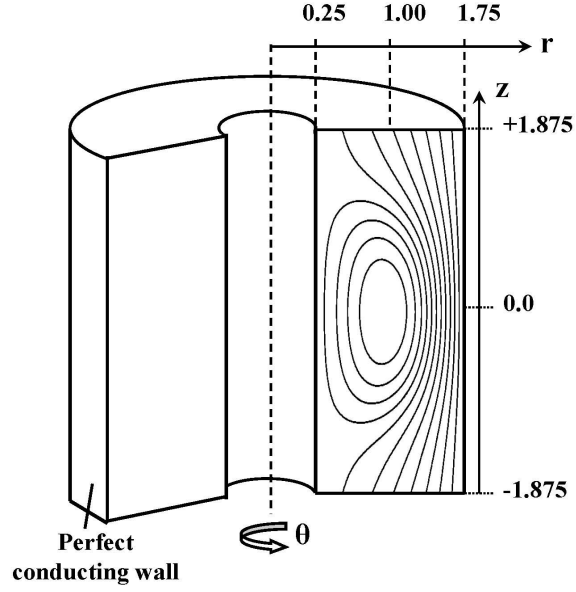


Figure 2.1: Schematic diagram of simulation geometry

and the outer boundaries. Therefore, we leave a sufficient margin in the vertical direction from the core plasma in order to avoid the disturbance from the reflection at the top and the bottom boundaries.

2.2 Physical models

2.2.1 MHD model

In order to analyze the dynamical behavior of the ballooning mode, we perform non-linear simulations based on the MHD model, where the plasma is treated as a single fluid with a single temperature. The independent variables are the mass density ρ ,

the fluid velocity \mathbf{v} , the magnetic field intensity \mathbf{B} , and the plasma pressure p . The time development of these variables is expressed by the standard set of the nonlinear resistive compressible MHD equations. The compressible nature in the governing equations is fully retained in the simulation model because of its importance in the nonlinear dynamics in this configuration.

$$\frac{\partial \rho}{\partial t} = -\nabla \cdot (\rho \mathbf{v}), \quad (2.1)$$

$$\begin{aligned} \frac{\partial}{\partial t} (\rho \mathbf{v}) = & -\nabla \cdot (\rho \mathbf{v} \mathbf{v}) - \nabla p + \mathbf{j} \times \mathbf{B} \\ & + \mu \left(\nabla^2 \mathbf{v} + \frac{1}{3} \nabla (\nabla \cdot \mathbf{v}) \right), \end{aligned} \quad (2.2)$$

$$\frac{\partial p}{\partial t} = -\nabla \cdot (p \mathbf{v}) - (\gamma - 1) (p \nabla \cdot \mathbf{v} + \eta j^2 + \Phi), \quad (2.3)$$

$$\frac{\partial \mathbf{B}}{\partial t} = -\nabla \times \mathbf{E}, \quad (2.4)$$

$$\mathbf{j} = \nabla \times \mathbf{B}, \quad (2.5)$$

$$\mathbf{E} = -\mathbf{v} \times \mathbf{B} + \eta \mathbf{j}, \quad (2.6)$$

$$\Phi = 2\mu \left(e_{ij} e_{ij} - \frac{1}{3} (\nabla \cdot \mathbf{v})^2 \right), \quad (2.7)$$

$$e_{ij} = \frac{1}{2} \left(\frac{\partial v_i}{\partial x_j} + \frac{\partial v_j}{\partial x_i} \right), \quad (2.8)$$

Equations (2.1) to (2.4) are the equation of continuity, the equation of motion, the equation of pressure, and the equation of induction, respectively. The current density \mathbf{j} is determined by Ampere's law (*i.e.*, (2.5)), and the electric field \mathbf{E} follows the Ohm's law (*i.e.*, (2.6)). The ratio of specific heats γ is 5/3 and for simplicity, the resistivity η and the viscosity μ are assumed to be uniform constant through out the whole region. The first term on the right hand side of (2.3) is the convection term and the heating terms like adiabatic compression, ohmic heating and the viscous heating are included in the second group of terms. By evaluating the viscous heating term Φ the system retains the local energy conservation among the plasma heat, the kinetic and magnetic field energies.

In the simulation, all the variables are treated as a normalized form, where the initial toroidal magnetic field at the magnetic axis, and the initial density which is assumed to be uniform in the initial state is set to be 1. since the pressure has the same order as that of energy density, (*i.e.*, $p_o = B_o^2$), pressure is automatically normalized by scaling magnetic field. The unit of the length is given by the major radius at the magnetic axis. Under these normalizations the velocity and the time are normalized by the Alfvén velocity at the magnetic axis and the transit time of the Alfvén wave on the axis, respectively. Therefore, we can compare the simulation results with real experiments, by scaling the spatial dimension, the density and the magnetic field. For

example, the plasma parameters of a typical NBI shot of the MAST plasma are given by the toroidal magnetic field at geometric center $\sim 0.52(T)$, the major radius $\sim 0.85(m)$, and the line average density $\sim 4.0 \times 10^{19}(m^{-3})$. By using these parameters, we can estimate the unit of the time scale for this shot as $1(\tau_A) \sim 0.47(\mu \text{ sec})$.

2.2.2 Simplified drift model

The MHD model is a useful approximation which has wide applicability for dynamical phenomena with Alfvénic spatio-temporal scales. The resistive version of this model can follow the processes which include the magnetic reconnection. However, the MHD approximation with a rigorous ordering estimation requires the target phenomenon to have the characteristic spatial scale sufficiently larger than the ion Larmor radius, and the time scale much shorter than the Alfvén one. The experimentally observed phenomena, even the explosive one like a hard disruption in tokamak, do not satisfy such conditions. As the first step to improve the modeling for more realistic situations, we examine the lowest-order modification on the MHD model by taking account of the FLR effect[85, 84]. In the fluid description, this corresponds to adding the ion diamagnetic drift velocity \mathbf{v}_p ,

$$\mathbf{v}_p = \frac{m}{2e} \frac{\mathbf{B} \times \nabla p}{\rho B^2} \quad (2.9)$$

to the standard MHD velocity, where m and e are the mass and the charge of the ion, respectively. By adding the advection term due to the diamagnetic rotation to the equation of motion (2.2), *i.e.*, we replace

$$-\nabla \cdot (\rho \mathbf{v} \mathbf{v}) \longrightarrow -\nabla \cdot (\rho \mathbf{v} \mathbf{v}) - \rho \mathbf{v}_p \cdot \nabla \mathbf{v} \quad (2.10)$$

therefore the modified equation of motion becomes

$$\begin{aligned} \frac{\partial}{\partial t} (\rho \mathbf{v}) = & -\nabla \cdot (\rho \mathbf{v} \mathbf{v}) - \rho (\mathbf{v}_p \cdot \nabla \mathbf{v}) - \nabla p + \mathbf{j} \times \mathbf{B} \\ & + \mu \left(\nabla^2 \mathbf{v} + \frac{1}{3} \nabla (\nabla \cdot \mathbf{v}) \right) \end{aligned} \quad (11)$$

$$(\mathbf{v}_p)_{\text{real}} = +\frac{m}{2e} \left(\frac{\mathbf{B} \times \nabla p}{\rho B^2} \right); \quad (\mathbf{v}_p)_{\text{sim}} = \zeta \cdot (\mathbf{v}_p)_{\text{real}} \quad (2.12)$$

a simple modification which includes the most essential part of the ion dynamics can be obtained. The ion diamagnetic drift velocity increases linearly with the dimensionless parameter ζ , where ζ is considered to be the controlling parameter. If we take $\zeta = 1$, it means we are using the realistic value of \mathbf{v}_p , however we also have used the exaggerated value ζ in order to investigate the effect of \mathbf{v}_p . More complete expression for the drift model was derived by Hazeltine and Meiss[71] and Chang and Callen[72] as the time development of the total velocity, including also the electron dynamics in the Ohm's law. However, the characteristic nature including the poloidal and toroidal diamagnetic rotation can be represented by our simplified model.

2.3 Initial equilibrium

Initial axisymmetric equilibria are obtained with the two-dimensional Grad-Shafranov equation in the poloidal plane (r, z) under the assumption of pressure and current profiles. We can derive the Grad-Shafranov equation from Ampere's law. First, as the current density j can be decomposed into components perpendicular and parallel to the magnetic field \mathbf{B} , we may write it in the following form;

$$\mathbf{j} = \mathbf{j}_\perp + \mathbf{j}_\parallel \quad (2.13)$$

where $\mathbf{j}_\perp = (\mathbf{B} \times \nabla p) / B^2 = (dp/d\psi) (\mathbf{B} \times \nabla \psi) / B^2$ and $\mathbf{j}_\parallel = j_\parallel \mathbf{B} / B$. After the vector manipulation, the current density become

$$\mathbf{j} = -r^2 \frac{dp}{d\psi} \nabla \phi - \frac{1}{\mu_o} \frac{dF}{d\psi} \mathbf{B} \quad (2.14)$$

When we take a dot-product of Ampere's law with $\nabla \phi$, the RHS becomes

$$\nabla \phi \cdot (\mu_o \mathbf{j}) = -\mu_o \frac{dp}{d\psi} - \frac{dF}{d\psi} \frac{F}{r^2} \quad (2.15)$$

and the LHS becomes

$$\begin{aligned} \nabla \phi \cdot (\nabla \times \mathbf{B}) &= \nabla \cdot (\mathbf{B} \times \nabla \phi) \\ &= \nabla \cdot (|\nabla \phi|^2 \nabla \psi) \\ &= \nabla \cdot \left(\frac{1}{r^2} \nabla \psi \right) \end{aligned} \quad (2.16)$$

As a result, the Grad-Shafranov equation becomes

$$\Delta^* \psi = -\mu_o r^2 \frac{dp}{d\psi} - F \frac{dF}{d\psi} \quad (2.17)$$

where

$$\Delta^* \equiv r \frac{\partial}{\partial r} \left(\frac{1}{r} \frac{\partial}{\partial r} \right) + \frac{\partial^2}{\partial z^2}$$

and ψ is a stream function for the poloidal magnetic field. In addition, the poloidal magnetic field B_R and B_z can be found in terms of cylindrical coordinates;

$$B_r = -\frac{1}{r} \frac{\partial \psi}{\partial z}, \quad B_z = \frac{1}{r} \frac{\partial \psi}{\partial r} \quad (2.18)$$

$p(\psi)$ and $F(\psi)$ are the two free function included in (2.17). In this simulation, the equilibrium pressure $p(\psi)$ is given by flux function,

$$p(\psi) = p_o (1 - (1 - \psi_n)^\alpha)^\beta \quad (2.19)$$

and the poloidal current function $F(\psi)$ is given by

$$F(\psi) = F_o (\psi_n^\beta + F_{ex}) \quad (2.20)$$

where ψ_n is the normalized poloidal flux function and is equal to unity at magnetic axis and zero at plasma vacuum boundary. α and β are constants and are chosen as $\alpha = \beta = 2$. The pressure profile is flat around the magnetic axis with $\frac{dp}{d\psi_n} = 0$ at the axis. Also $F(\psi)$ is related to the toroidal magnetic field by

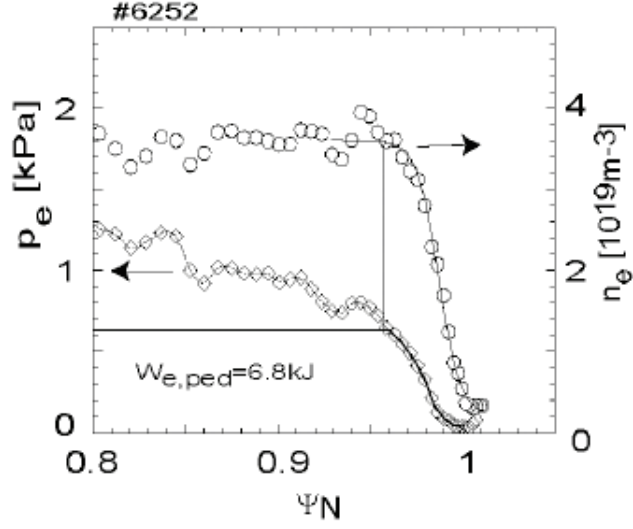


Figure 2.2: Electron density n_e , pressure p_e and energy pedestal $W_{e,ped}$ in a quasi-stationary ELMy H-mode discharge (#6252) [57].

$$B_\theta = -\frac{1}{r}F(\psi) \quad (2.21)$$

$\psi(r, z)$ at equilibrium state is obtained by solving (2.17) numerically on the poloidal cross section. and further the solution of $\psi(r, z)$ is substituted in (2.18), (2.19) and (2.20) to calculate two dimensional magnetic field ($B_{GS}(r, z)$) and pressure ($p_{GS}(r, z)$) at equilibrium state.

After calculating numerically the two dimensional equilibrium from the procedure mentioned above, we extended the equilibrium into the three dimensional axisymmetric field quantities by the following equations,

$$B(r, \theta, z) = B_{GS}(r, z) \quad (2.22)$$

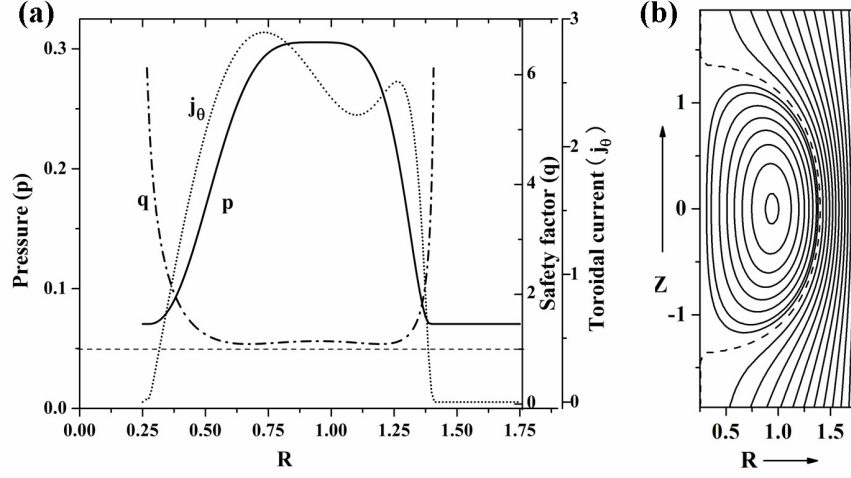


Figure 2.3: Initial condition of the simulations. (a) Radial profiles of the plasma pressure(p), the net toroidal current(j_θ), and the safety factor(q). (b) Contour map of poloidal flux. The position of the separatrix is indicated with dashed line.

$$p(r, \theta, z) = p_{GS}(r, z) + p_{bias} \quad (2.23)$$

Here we suppose that the outside region of the separatrix is filled with uniform low pressure plasma. This treatment is done by adding a low biased pressure to $p_{GS}(r, z)$ as shown in (2.23) uniformly. Since the motion of plasma as shown earlier in (2.2) is dependent on gradient of pressure (*i.e.*, ∇p), therefore by adding low uniform pressure all over the simulation will not break the equilibrium condition. Such treatments helps to avoid negative pressure and continue the simulation smoothly even in highly nonlinear regime. Thus we add 20% of the maximum pressure as p_{bias} . The initial mass density is assumed to be uniform *i.e.*, $\rho(r, \theta, z) = 1$. Shown in Fig. 2.3(a) is the radial pressure (p), net toroidal current (j_θ), and safety

factor (q) profiles. The profiles are selected to be moderately broad in the core region, following the conventional experiments (i.e., see Fig.2.2 [57]), where the aspect ratio $A = 1.5$, the elongation $\kappa = 2.1$, the q value at the magnetic axis is $q_0 = 1.146$, minimum value of $q_{min} = 1.093$, and the central plasma beta $\beta_0 = 46.9\%$. The contour of the poloidal flux of the initial equilibrium are shown in Fig. 2.3(b). The position of the separatrix is identified by dotted line.

2.4 Boundary condition

Our simulation region consists of the following boundaries, the inner boundary ($r = r_{min}$), the outer boundary ($r = r_{max}$), the top ($z = z_{min}$) and bottom ($z = z_{max}$) boundaries. The real boundaries in the experiments, are usually made of metal, therefore if we ignore the complicated effect like recombination, the secondary electron, the reflected backward flow of plasma, and impurity etc, then the most reasonable condition for the boundary is the perfect conducting. Foreexample the center rod in ST is made of metal therefore the inner boundary is treated as conducting wall by introducing B_{\perp} as constant on the relevant component of the magnetic field at the innermost mesh for each time step. Hence we assume the perfect conducting no-slip wall as boundary condition for the outer, inner, the top, and the bottom boundaries. However in the toroidal direction it is periodic in nature.

2.5 Numerical scheme

Numerical calculation of the MHD model equation and Drift model equation has been implemented by using finite difference method and Runge-Kutta method. In the current simulation the numerical grid is composed of r , θ , and z direction. The grid numbers are chosen to be $(N_r, N_\theta, N_z) = (128, 64, 256)$, which is large enough to treat the current problem. The finite difference method (FDM) consists of transforming the partial derivatives in difference equations over a small interval. To obtain as higher accuracy as possible with reasonable memory size, it is effective to raise the order of finite difference approximation. The spatial derivatives on the right hand side of (2.1) – (2.4) are approximated by using fourth-order finite differences scheme. A first spatial derivative of a variable f at a discrete point is represented in the fourth order central difference form by

$$\frac{\partial f}{\partial x}|_{x=x_i} = \frac{1}{12\delta x} (-f_{i+2} + 8f_{i+1} - 8f_{i-1} + f_{i-2}) \quad (2.24)$$

where i is the index of numerical grid for spatial coordinate x , and δx is its interval. The numerical error due to finite difference approximation is of the order of $(\delta x)^4$ at most. Since (2.24) needs information of two neighbors at both directions *i.e.* $i - 2$ and $i + 2$, therefore another treatment is necessary near the boundaries. To treat such a problem we adopted another approach, which makes use of a lower order approximation near the boundaries. Such treatment of reducing the order has a stabilizing effect for the solution particularly when there is reflection of short wavelength waves at the

boundary wall. Therefore the grid points next to boundary is treated with a second order central difference scheme,

$$\frac{\partial f}{\partial x}|_{x=x_i} = \frac{1}{2\delta x} (f_{i+1} - f_{i-1}) \quad (2.25)$$

and, at the boundary, a first order difference is used.

$$\frac{\partial f}{\partial x}|_{x=x_i} = \frac{1}{\delta x} (f_{i+1} - f_i) \quad (2.26)$$

Thus all the derivatives in the RHS of the (2.1) – (2.8) are represented in the finite difference form by using (2.24) – (2.26). The partial differential equations are now treated as ordinary differential equations in respect of t by estimating the right hand side at each time.

The time advancement of MHD equations is performed by using an explicit fourth-order Runge-Kutta scheme. It is one of the standard algorithm to solve differential equations. Now we denotes the set of the independent variables $(\rho, \mathbf{v}, \mathbf{B}, p)$ by the vector \mathbf{y} , and the sum of the RHS of (2.1) – (2.4) by vector \mathbf{g} . The fourth order Runge-Kutta requires four gradient or \mathbf{k} terms to calculate \mathbf{y}^{n+1} ,

$$\mathbf{k}_1 = \delta t \mathbf{g}(\mathbf{y}^n) \quad (2.27)$$

$$\mathbf{k}_2 = \delta t \mathbf{g}\left(\mathbf{y}^n + \frac{\mathbf{k}_1}{2}\right) \quad (2.28)$$

$$\mathbf{k}_3 = \delta t \mathbf{g} \left(\mathbf{y}^n + \frac{\mathbf{k}_2}{2} \right) \quad (2.29)$$

$$\mathbf{k}_4 = \delta t \mathbf{g} (\mathbf{y}^n + \mathbf{k}_3) \quad (2.30)$$

$$\mathbf{y}^{n+1} = \mathbf{y}^n + \frac{1}{6}(\mathbf{k}_1 + 2\mathbf{k}_2 + 2\mathbf{k}_3 + \mathbf{k}_4) \quad (2.31)$$

where n and δt is the time index and the time interval respectively. Combining (2.1) – (2.4) and (2.27) – (2.31), can solve the MHD equations numerically. In case of drift model equations, (2.2) will be replaced with the (2.11), the rest of procedure is the same as mentioned for MHD equations.

Chapter 3

MHD simulation results

3.1 Overview of simulation results:

In this chapter, the nonlinear dynamics of the ballooning mode are presented by means of numerical simulations in the framework of MHD model. With the given equilibrium similar to the conventional experiments, the nonlinear simulations are executed in a three dimensional full toroidal geometry. In the linear analysis, the intermediate- n modes have larger growth rates than others. These intermediate- n modes have a ballooning mode nature, the mode structures are poloidally localized in the bad curvature region, and have a wide envelope consisting of several poloidal components. In the nonlinear phase, the MHD ballooning modes evolve into a nonlinear structure that results in the formation of a number of hot plasma filaments, elongated along a magnetic field line, but localized about it. These filaments extend out into the scrape-off layer on the outboard side but remain connected back into the pedestal region on the inboard side. These results are compared qualitatively with the experimental observation of the ELMs in MAST and NSTX experiments. Good agreement is found in the following characteristics of filaments: presence of intermediate- n precursors, triggering by the ideal ballooning mode, formation and

separation of filaments from the core plasma, non-uniform growth of filaments, time scale of ELM crash, and loss of plasma through convective process.

3.2 Linear instability

3.2.1 Linear growth of instability

In the initial equilibrium as shown in Fig. 2.3, the pressure profile is somewhat broad in the core region, and steeply falls at the edge, where the ballooning modes can be easily destabilized. The q profile, on the other hand, does not include the $q = 1$ rational surface over the whole poloidal cross section, and is set to be slightly greater than 1 at the core, whereas in the edge region, the q value increases rapidly toward the plasma surface. Therefore, various kinds of ballooning modes which are resonant to the neighboring rational surfaces can be destabilized simultaneously in the edge region.

By adding tiny random perturbations to the velocity components in the initial equilibrium as the seed of the instability, the system begins to develop spontaneously. The perturbations grow exponentially with several kinds of eigenmodes. Figure 3.1(a) shows the time development of the magnetic energy for each toroidal Fourier mode for the MHD case. Note that the intermediate- n modes are linearly unstable in the early phase, with intermediate- n have larger growth (especially, $n = 9$). The low- n (*i.e.*, $n < 4$) and high- n modes (*i.e.*, $n > 11$) are nonlinearly driven as

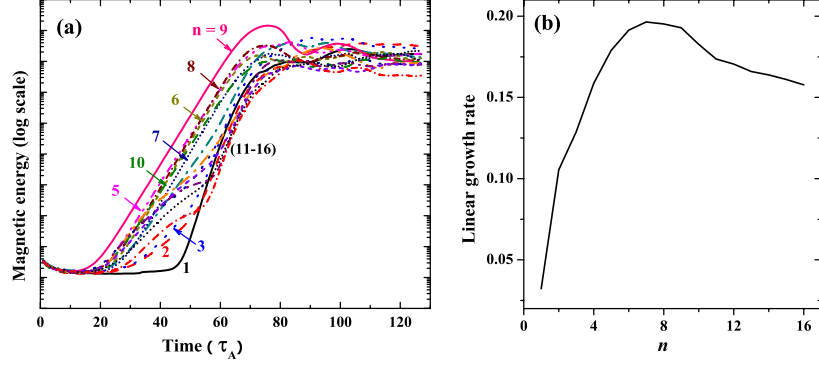


Figure 3.1: (a) Time development of magnetic energy for each toroidal Fourier component n . (b) The linear growth rate for each toroidal Fourier mode number n .

the intermediate- n acquire finite amplitude. The exact toroidal mode structures can be obtained from the simulation based on the linearized version of (2.1) – (2.4). Figure 3.1(b) shows the linear growth rate (γ_n) for each toroidal mode and is estimated by using $\gamma_n = \frac{1}{2} \frac{\Delta(\ln E_m)}{\Delta t}$, where E_m is the magnetic energy of the perturbation at time t . It is shown that the intermediate- n modes have larger growth rate, especially, the $n = 5 - 9$ components have peaks for the ideal ($\eta = 0$) case. Hence the nonlinear activity will be dependent on the intermediate modes. In the later stage, after $t = 50\tau_A$, the mode coupling effects become significant and higher- n and lower- n are seen to be excited. This stage may be called the nonlinear stage.

3.2.2 Linear mode structures

In this section, we discuss the detail of the linear mode structure of the linear instability. Shown in Fig. 3.2 is the poloidal mode structures of such instabilities with two-dimensional color image contours of the perturbations in the pressure, and with the radial profiles of the poloidal Fourier expansions of the magnetic field energy. Figure 3.2(a) shows the poloidal cross-section of the fluctuation component in the pressure for the dominant toroidal mode (*i.e.*, $n = 9$). The dotted line shows the position of rational surface. The red and blue contour denotes the positive and negative perturbation in pressure respectively. The region where the pressure fluctuation becomes positive corresponds to the region where the plasma flow is gathered. It shows that these modes are poloidally localized in the so-called bad-curvature region with unstable mode peaks in the outboard side of plasma. This is the most noticeable supporting evidence of the ballooning mode because the growth of the mode is affected by the magnetic field curvature. This is shown in Figure 3.2(b), it shows the poloidal Fourier expansion of the magnetic field energy. It shows wide envelopes with multiple poloidal components, causes a helically extending expansive deformations at the plasma surface. This is also typical behavior of ballooning modes.

Another analysis for the evaluation of the free energy source by using the energy principle as given by (1.3), is presented in Table (3.1). As mentioned earlier the first three term appear in the RHS of (1.3) corresponds to the change in the potential energy of the Alfvén wave, the fast magneto-acoustic wave, and the acoustic wave.

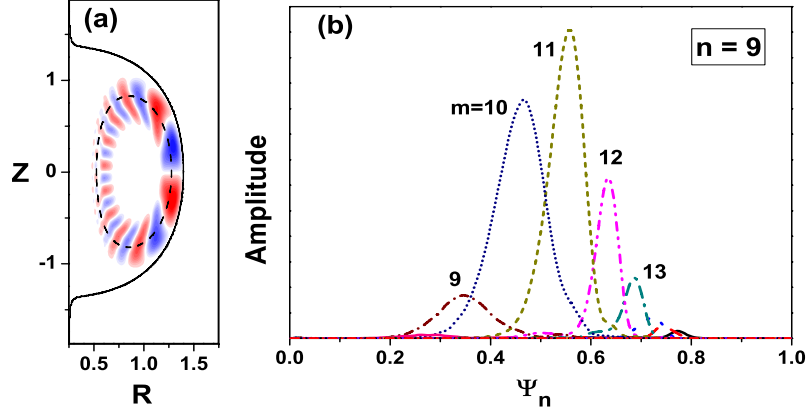


Figure 3.2: Poloidal mode structure of the linear $n = 9$ mode. (a) color contour map of the perturbations in p on a poloidal cross section. Thick line indicates the location of the separatrix. (b) Radial profile of the perturbation amplitude in the magnetic energy for each poloidal Fourier mode number m . The horizontal axis indicates the normalized poloidal flux from the magnetic axis ($\Psi = 0$) to the separatrix ($\Psi = 1$).

These terms are positive definite, so that they have a stabilizing effect. The fourth and fifth term are related pressure driven and the current driven instability respectively. Both the current-driven and the pressure-driven terms come out to be negative for intermediate- n (*i.e.*, $n = 5, 6, 8$ and 9). Therefore, the instability is driven by the combination of the effect of both the current and the pressure gradient. Furthermore, it can be seen that the pressure-driven term is much larger than the current-driven term for intermediate- n . Therefore, we can conclude that the instability has a nature of the pressure-driven modes for intermediate- n .

As for the effect of the resistivity, the obtained η dependencies of the growth rate for each toroidal mode has been shown in Fig. 3.3. It shows that for $\eta \leq 1 \times 10^{-5}$

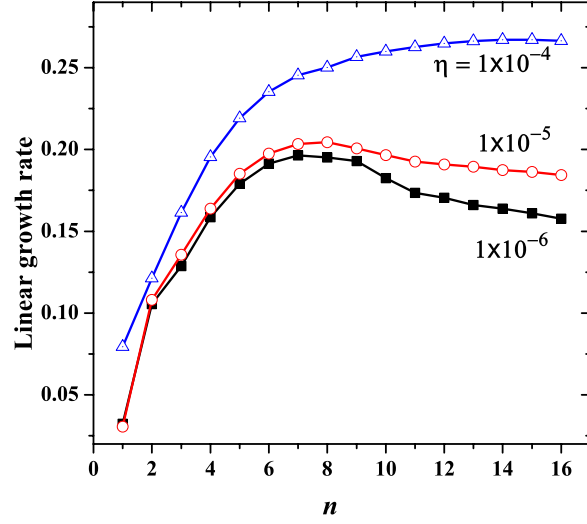


Figure 3.3: The resistivity η dependence of the linear growth rate for each toroidal Fourier mode number n .

Terms	$n = 5$	6	8	9
Kink	-1.0	-1.0	-1.0	-1.0
Ballooning	-6.0	-8.4	-15.7	-21.1
Alfvén	4.5	5.8	9.6	11.8
Fast magneto acoustic	0.77	1.1	2.5	2.4
Acoustic	0.76	1.2	2.9	3.4
Total	-0.97	-1.3	-1.7	-4.5

Table 3.1: Estimation of the change in total potential energy by using the energy principle. All the terms are normalized by the absolute value of the kink term for each mode.

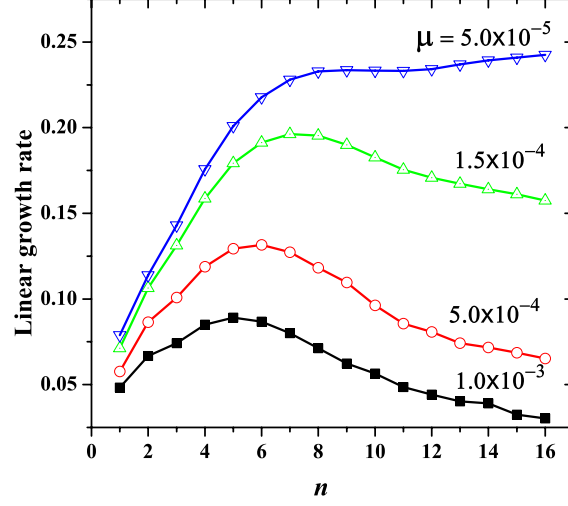


Figure 3.4: The viscosity μ dependence of the linear growth rate for each toroidal Fourier mode number n .

, there is no significant change in the growth rate. Therefore, it can be identified that these modes are mainly ideal in nature for those parameter ranges. We hereafter adopt $\eta = 1 \times 10^{-5}$ for the rest simulations. Incidentally, as shown in Table 3.1, the sum of all terms is really negative, it means that these modes are ideally unstable. It also supports the conclusion that these modes are ideal mode. Hence from Fig. (3.2 and 3.3) and Table 3.1 we can conclude that the modes which are currently under investigation are ideal ballooning modes in nature.

Figure 3.4 shows the growth rate for each mode defined by Fig. 3.1(a) for different value of viscosity (i.e., $\mu = 5 \times 10^{-5}$, 1.5×10^{-4} , 5×10^{-4} , and 1×10^{-3}). It can be seen clearly that with the increase of viscosity, the dominant modes

shift toward intermediate- n value, and the dampness of higher- n modes becomes prominent. On the other hand for small viscosity i.e., 5×10^{-05} the damping of higher- n by viscosity is not effective, so that growth rate for each mode is larger than that of 1.5×10^{-04} and higher μ value. Such high- n activity cannot be treated properly in our simulation which use a finite difference scheme in a discrete numerical grid system because of lack of numerical grid. Besides, experimentally, the intermediate- n activity is thought to play more important role as a precursor to the ELM in ST. Therefore, our simulation should also focus on such intermediate- n activity. The viscosity should be set to be large well enough to damp the high- n modes in linear phase. Too large viscosity, such as 5×10^{-04} , and 1×10^{-03} , however, will cause an undesirable damping and saturation of growth. Thus, we use an appropriate value for the viscosity of i.e., 1.5×10^{-04} for Fig. 3.1(a).

3.3 Nonlinear dynamics

3.3.1 Formation of filamentary structure

In this section we will investigate the dynamical behavior of ST plasma in the nonlinear stage. As we can see from Fig. 3.1(a) the instability keeps growing linearly with the growth rate till $t = 50\tau_A$. This is the time when we see the first indication of non-linearity when there is abrupt change in the growth rate of high- n mode (i.e., 11 – 16)

that are driven as the intermediate- n modes acquire finite amplitude. Hence the hyper harmonics of the linear eigenmodes are excited abruptly and grows strongly. After this time some of the perturbations are dissipated and others coalesce into larger balloons. Thus, the growth of the instability is saturated and the perturbations become visible scale as shown in Fig. 3.1(a).

Shown in Fig. 3.5(a) is the time development of the 2D pressure profiles in a poloidal cross section on the early nonlinear stage. One can see the plasma surface dimples with a substantial scale at $t = 70\tau_A$. Especially, a large balloon is formed in the outer edge region, whereas the inner edge is disordered in small scale fragments, reflecting the local pitches of the field lines. On the other hand, the core region roughly keeps its initial profile, since the relevant ballooning modes are localized only in the edge region. At $t = 80\tau_A$ (*i.e.*, the highly nonlinear phase) some of the balloons are separated from the core plasma, and ejected into the open field region. Such a time development is also represented with a three-dimensional iso-pressure surface in Fig. 3.5(b). The ejection process of the balloons can be clearly seen. The balloons are formed in helically twisted shapes along the magnetic field at $t = 70\tau_A$. The balloons are separated from the core as a plasmoid or filament at $t = 80\tau_A$ in a thin arch shape which extends from the top and bottom of the torus. The filament looks belt like structure with $n = 9$ as the dominant mode and is moving away from the plasma edge perturbing the SOL region.

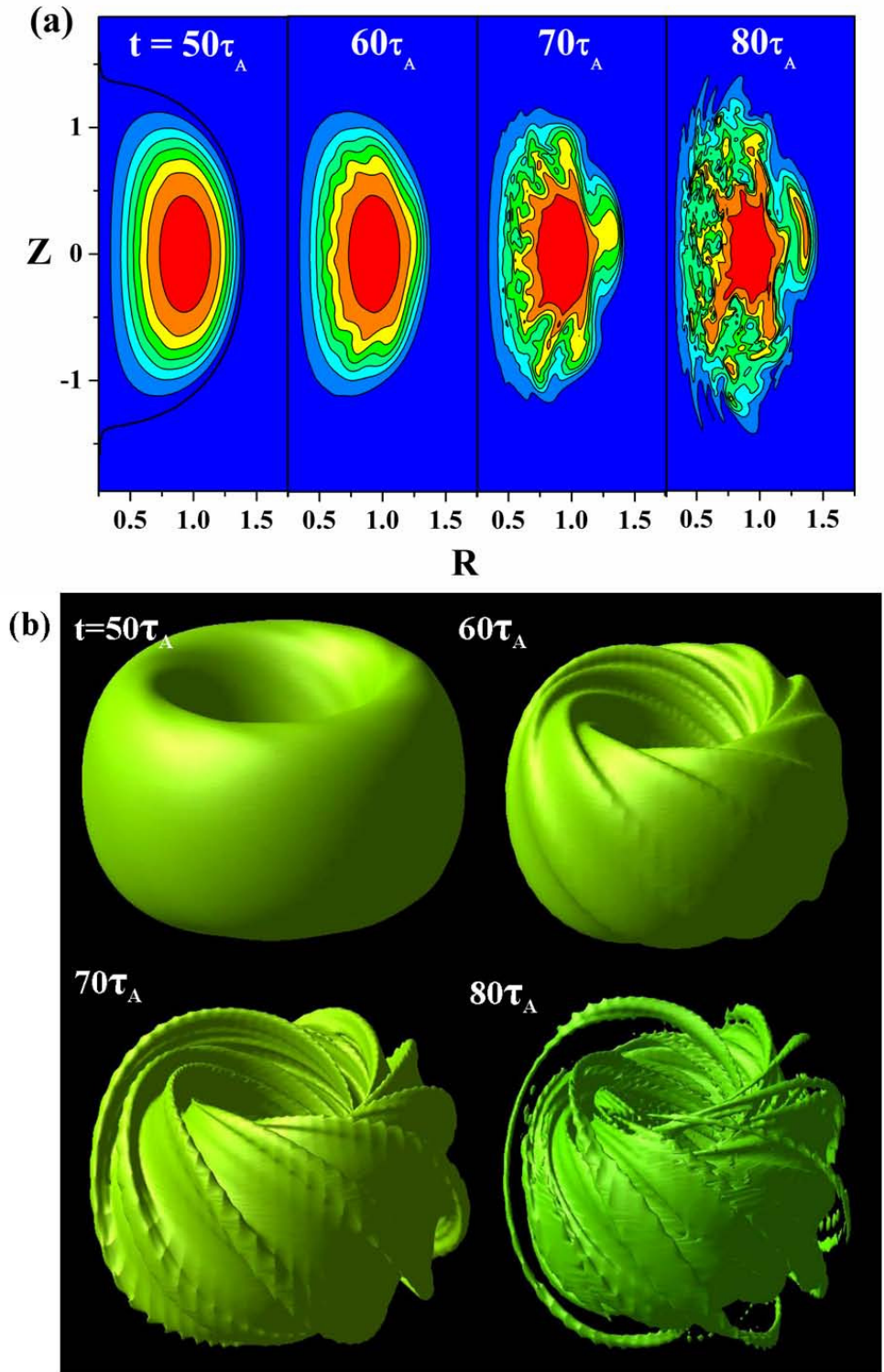


Figure 3.5: Nonlinear time development of the pressure profile represented with (a) image contour map of the net pressure(p), and (b) 3-D bird's-eye view of an iso-pressure surface.

3.3.2 Non-uniform growth of filament

Figure 3.6(a) shows a top view of a three-dimensional iso-contour surface of pressure at $t = 76\tau_A$. Note that the filamentary structure erupts only from few prominent balloons regardless of the dominant linear mode numbers. In order to explore this we plotted different combination of the dominant toroidal mode numbers $n = 9$ (red), 6 (green) and 5 (blue). For further detail see Fig.3.6(b), where $n = 9$ and 5 are plotted. If one compare this with the previous figure, the filaments erupt only on those balloons where there is a positive alignment of $n = 9$ and $n = 5$ modes. Fig.3.6(c) and (d) shows the 9, 6 and 5, 6 combination. And if we compare this with Fig.3.6(b) it is clear that coupling of $n = 9$ and 5 is much stronger as compare to the rest of combination. This can be explained by the position of rational surface for $n = 9(m/n = 11/9 = 1.22)$, $6(m/n = 7/6 = 1.16)$ and $5(m/n = 6/5 = 1.2)$. The rational surface of $n = 9$ and 5 are located much closer as compare to $n = 9, 6$ and $6, 5$ combination, enhancing the probability of strong toroidal coupling. Thus such nonlinear coupling of the dominant toroidal modes results in nonlinear growth of filament.

3.3.3 Field line behavior

In this section we will investigate the behavior of magnetic field line as well as the flow pattern of stream lines. The field line structures on this stage are shown in Fig. 3.7. The semi transparent surface indicates the iso-contour of plasma pressure,

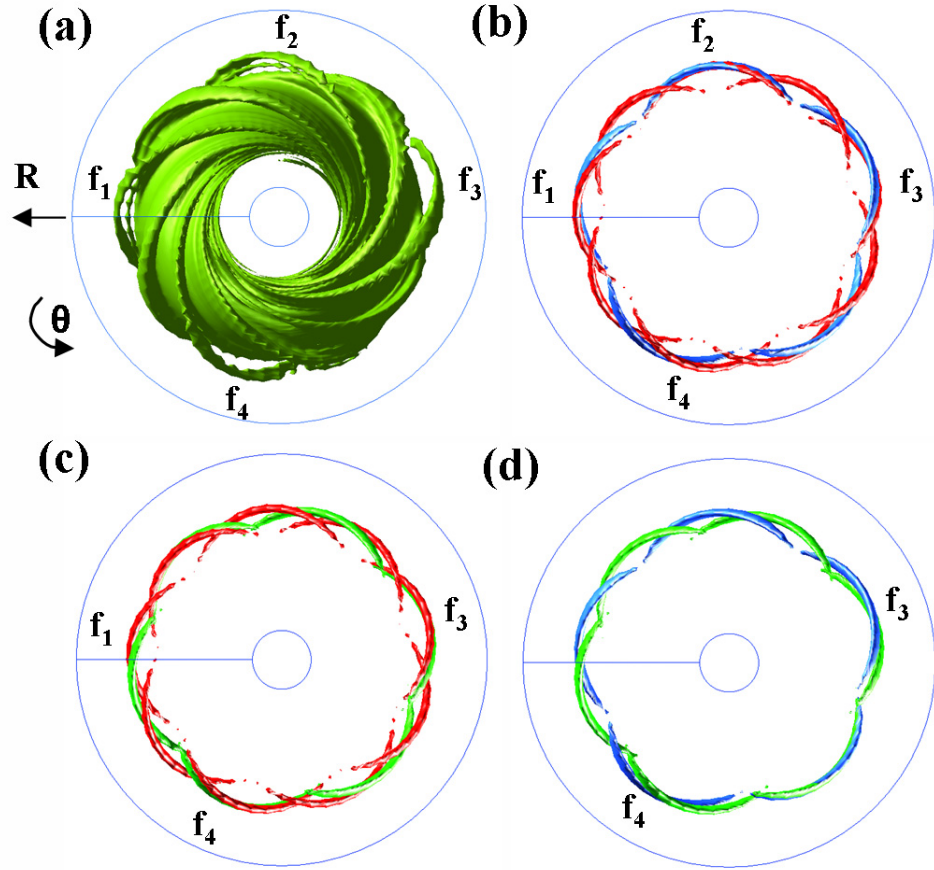


Figure 3.6: (a) Top view of a three-dimensional iso-contour surface of net pressure at $t = 76\tau_A$. It shows the nonlinear growth of few localized filaments. The filaments are identified as f_1, f_2, f_3 and f_4 . The number of filaments are much less than the number of dominant toroidal mode (i.e. $n = 9$). The perturbation component in pressure for (b) $n = 9$ (red) and 5 (blue), (c) $n = 9$ (red) and 6 (green) and (d) $n = 5$ (blue) and 6 (green) Fourier components are plotted together. It shows the alignment of $n = 9$ and 5 perturbation in the direction of localized formation of filamentary structure f_1, f_2, f_3 and f_4 are much stronger than case (c) and (d) combination.

the arbitrary traces of the magnetic and the plasma flow field lines are represented in blue and red, respectively. This structure is correspondent with the convection motion of the plasma flows, which forms a twin-vortex pattern as clearly seen from the early nonlinear stage at $t = 60\tau_A$ as shown in Fig. 3.7(a). The stream lines along each side of the finger flows spirally in such a way that at the center of each finger, the velocity field moves outward along the radial direction, pushing the core plasma from inside to outside. At $t = 68\tau_A$, more prominent balloons appears on the plasma pressure iso-surface. The stream lines still have a twin vortex flow pattern around each finger. This figure also helps us to visualize how the ballooning structure looks like. In this figure we showed two type of field line, one coming from inside, and the other along the outside surface. The filament erupts on inner surface along the field line and moves radially outward. Most probably the field line on the outside surface allows the field lines from inside to pass through. At $t = 80\tau_A$, we observe the eruption of the filamentary structures, roughly following the magnetic field lines on the plasma surface. Although at this point it is difficult to trace the stream lines along the finger because of highly nonlinear regime but still we observed single spiral motion on the top and bottom of the filament. The twin vortex flow pattern is no more observable because the filament is separated from the plasma edge in radial direction.

The twin-vortex flow pattern is more clearly shown in Fig. 3.8 with a two-dimensional toroidal flow pattern on the mid plane. One can see that the balloon ridge is formed along the spouting out of the plasma flows. When the balloon is

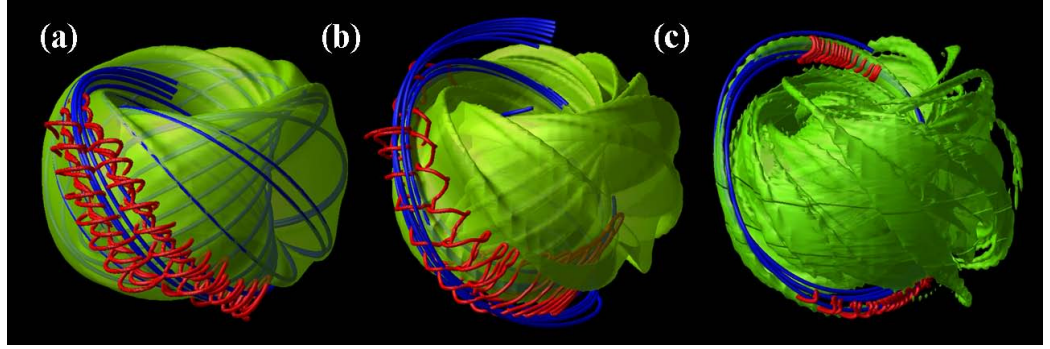


Figure 3.7: Time evolution of plasma pressure iso-contour (green), the arbitrary traces of magnetic field line (blue), and the stream line (red) at (a) $t=60\tau_A$ (b) $t=68\tau_A$ and (c) $t=80\tau_A$. Stream lines makes twin vortex structure along the finger in early nonlinear phase. The magnetic field line extended along the filamentary structure.

formed at the plasma surface, the magnetic field lines on both sides of the separatrix are pushed against each other by such perpendicular flows due to the spouting-out. Under this situation the reconnection of the field lines can effectively occur by the driven reconnection mechanism[77]. In Fig. 3.9(a), two bunches of the magnetic field lines are drawn. The upper one is traced from the points in the external open field, where no field line was connected to the inside of the separatrix at the initial state. However, at $t = 82\tau_A$ the field line trace penetrates the separatrix, and connected to the internal toroidal field. This proves that the reconnection occurs somewhere along the trace, possibly, at the ridge of the balloon. This type of the reconnection is also observed in our previous simulation for the IRE in ST[78, 80]. Once such reconnection occur, the plasma rapidly flows out through the reconnected field lines due to the parallel pressure gradient. After the internal free energy is partially lost by such convective processes, the system ceases to develop and reaches a relaxed state.

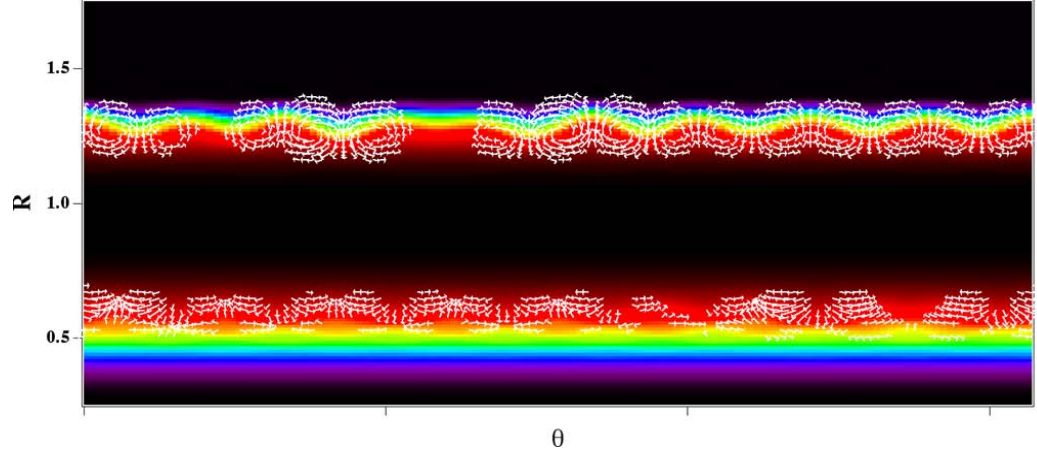


Figure 3.8: Toroidal flow pattern on the equatorial plane at $t = 60\tau$. The plasma toroidal flow velocity is represented by fine arrows. The color contour map indicates the plasma pressure, where the color varies from blue, green, red, to black as the pressure increases.

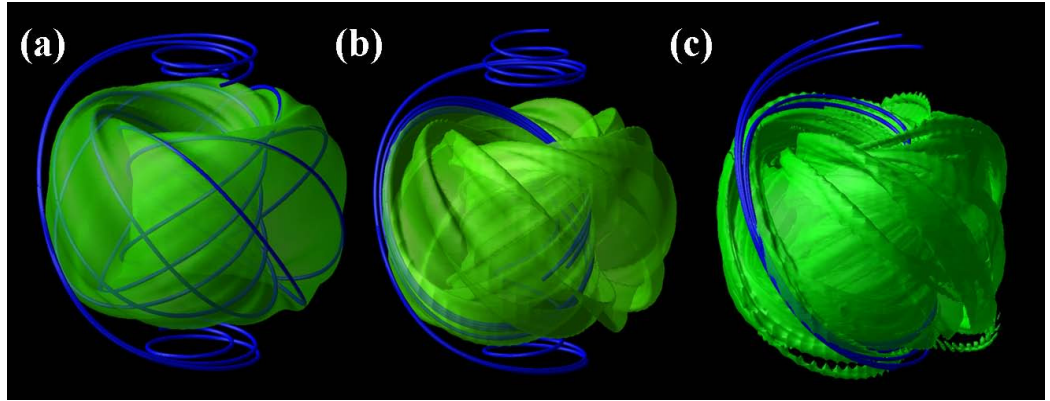


Figure 3.9: Magnetic reconnection between internal and external field. An identical magnetic field and an iso-pressure surface near the separatrix are drawn for (a) $t = 60\tau_A$ (b) $t = 68\tau_A$ and (c) $t = 82\tau_A$.

Chapter 4

FLR effects

In the second part of our simulation, we introduced the finite Larmor radius (FLR) effects in MHD equations also called as drift model, which can play significant part in the pedestal region. The drift model simulations follow the dynamics in a more realistic manner by introducing a global rotation of the perturbations in both toroidal and poloidal directions. These rotations are introduced in the MHD momentum equation through the advection term due to the ion diamagnetic drift effect. The simulation results in the linear phase show the suppression of the higher wave number components due to sheared rotational flows. In the nonlinear phase, however, filament separation processes are found to take place universally with and without FLR effect. The nonlinear flow pattern for the drift model shows the formation of single vortex pattern, which is in contrast with the MHD case. However, the overall nonlinear time development shows unexpectedly similar behavior for both cases. Therefore, the formation mechanism of the filamentary structure separating from the core plasma seems not to be related to the vortex motion of the balloon structure but dependent on the MHD nonlinear terms. It should be noted that in any cases clear extended balloon structure (finger) emerges on the plasma surface and separate from the core as filaments. Thus, the dynamics for the eruption could be determined only by the MHD terms.

4.1 Linear instability

In this section we executed the drift model simulation by using (2.10) under the same geometry and with the same initial condition as described in Sec. (2.3). We found dramatic and more realistic changes in the growth rate in the linear phase after the inclusion of the lowest order finite Larmor radius correction. Physically, FLR effects introduce a drift wave that propagates transverse to the magnetic field and pressure gradient. This drift convects the perturbations along the pressure gradient, for sufficiently large drift the perturbation phase mix with in growth period and provide small cutoff to unstable high- n ballooning modes. For the experimental parameter($\zeta = 1.0$), some exaggerated ones($\zeta = 2.5, 5.0, 7.5$), and the MHD($\zeta = 0$) cases, the simulation have been executed. The advection term added in the equation of motion introduces a global rotation of the perturbations both in toroidal and poloidal directions. Figure 4.1 shows the \mathbf{v}_p field structures in the poloidal cross section. One can see that a narrow flow shear band exists in the edge region.

Shown in Fig. 4.2 and 4.3 are the time development of the perturbation in magnetic energy of each toroidal Fourier mode (*i.e.*, $n = 1 - 16$) for different value of ζ (*i.e.*, 1.0, 2.5, 5.0, and 7.5). In case 1 as shown in 4.2(a), when $\zeta = 1$, which also gives the realistic value of \mathbf{v}_p , although the time development of magnetic energy is very much similar to the MHD simulation but still we found small suppression for $n > 6$ in linear phase. The $n = 9$ is still the dominant toroidal mode in the linear phase, however $n = 5$ becomes dominant as the simulation enters the nonlinear

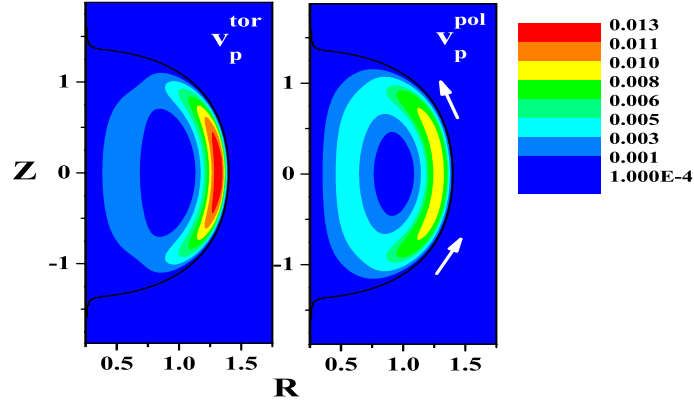


Figure 4.1: Image contour of the (a) toroidal and (b) poloidal diamagnetic drift speed on a poloidal cross section for the drift model simulation with $\zeta = 1$.

phase. By raising the value of ζ to exaggerated value of 2.5, the suppression becomes more prominent in linear phase as shown in Fig.4.2(b). In this case the number of dominant toroidal modes shift from higher to intermediate number (*i.e.* $n = 5$ and 6 are the dominant modes with a clear suppression of $n = 9$ mode in the linear phase). If we increase the value ζ further to intermediate levels *i.e.*, 5.0 (see Fig. 4.3(a)), we observed a suppression of even $n = 5$ but still $n = 5$ is dominate among the rest of the intermediate and high modes. There is a clear suppression of $n = 9$ modes during the linear phase where as in the nonlinear phase $n = 9$ excited abruptly this behavior looks similar to previous plots when higher modes *i.e.*, $n > 10$ grows abruptly because of the coupling of intermediate modes. In the fourth simulation we tested the

$\zeta = 7.5$, which is 7 times the realistic value of ζ for \mathbf{v}_p . For such higher value of ζ , the time development of magnetic energy is totally different then the MHD case. In the linear phase the low- n are dominant, where as the intermediate and higher modes are highly suppressed. We can estimate easily the linear growth rate from the behavior of perturbation in magnetic energy plot, However the toroidal mode spectra, which are plotted in Fig. 4.4 with ζ dependencies of the growth rate are estimated by using the linearized version of the drift model equations. It shows that the higher- n components are effectively suppressed by increasing ζ . last case when we perform simulation with even higher value of ζ (*i.e.*, 7.5), the FLR term played a more dominant role in suppression of even the intermediate- n , which were not stabilized with smaller concentration of ζ . The above four simulation results shows that FLR-MHD clearly grows slower then the MHD, the higher modes do not grow linearly, in contrast to MHD simulation where modes $n = 5 - 9$ appears to be the dominant mode.

4.1.1 Rotation of modes structure

The growth of the eigenmodes is affected by the diamagnetic rotation of the bulk plasma through the modified advection term. It can be clearer if one see the poloidal mode behavior. Figure 4.5 shows the time development of the perturbations in the poloidal pressure profile for the $n = 5$ component of the $\zeta = 5.0$ case. As one can see, the poloidal mode structure has a similar ballooning type profile to that for the MHD case. However, for the $\zeta = 5.0$ case, the mode structure rotates in the poloidal

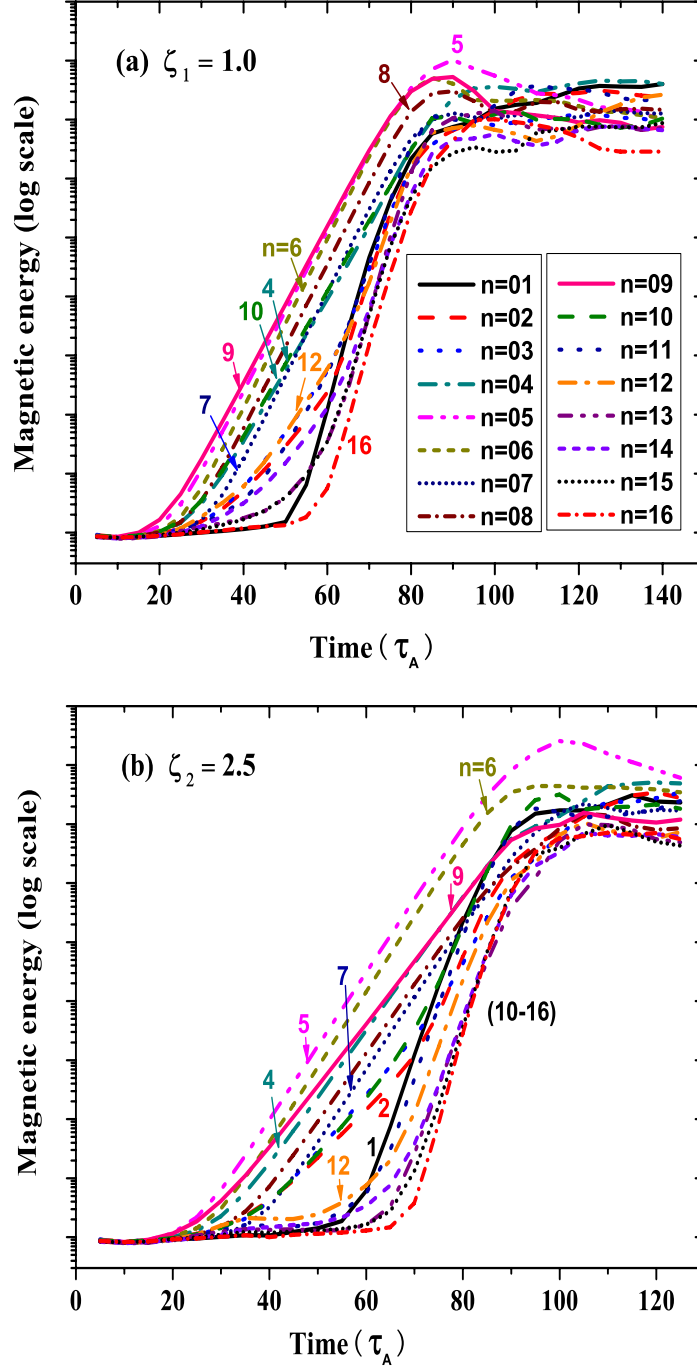


Figure 4.2: Time development of magnetic energy for each toroidal Fourier component n for small ζ (a) $\zeta = 1.0$ and (b) $\zeta = 2.5$.

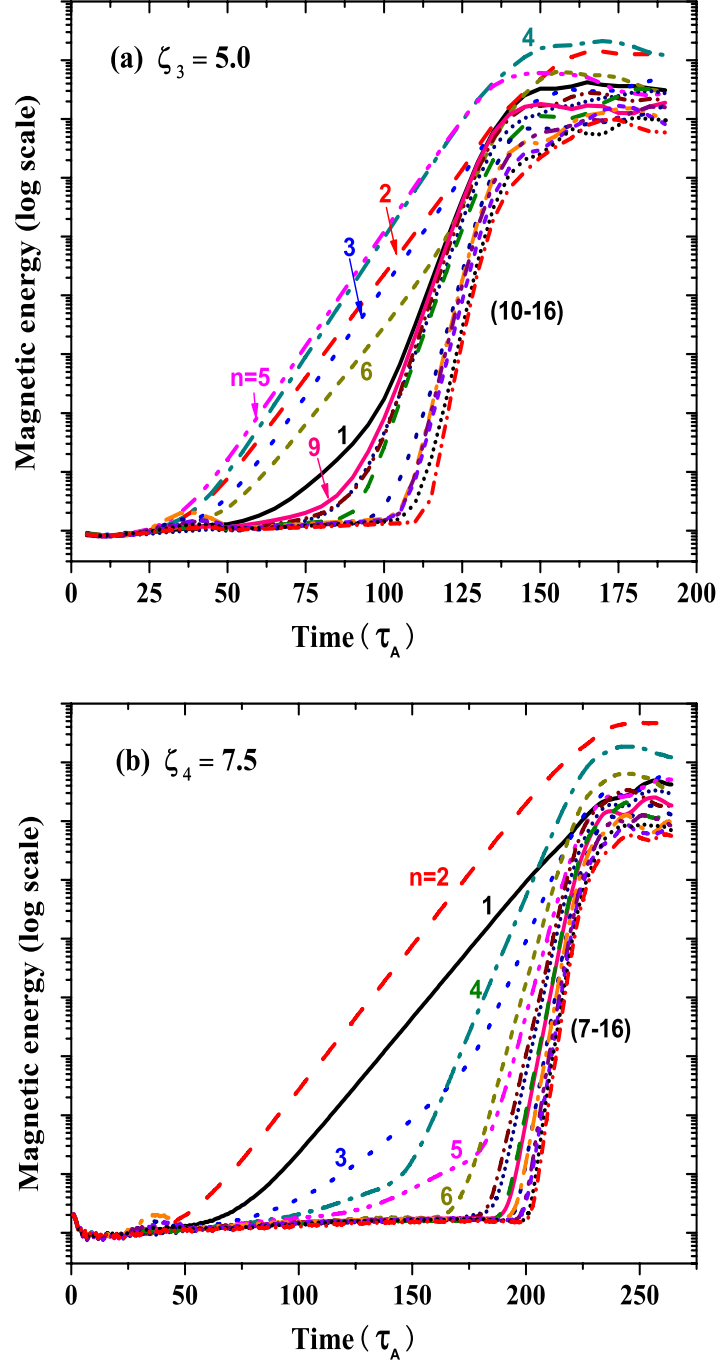


Figure 4.3: Time development of magnetic energy for each toroidal Fourier component n for intermediate and high value of ζ : (a) $\zeta = 5.0$ and (b) $\zeta = 7.5$.

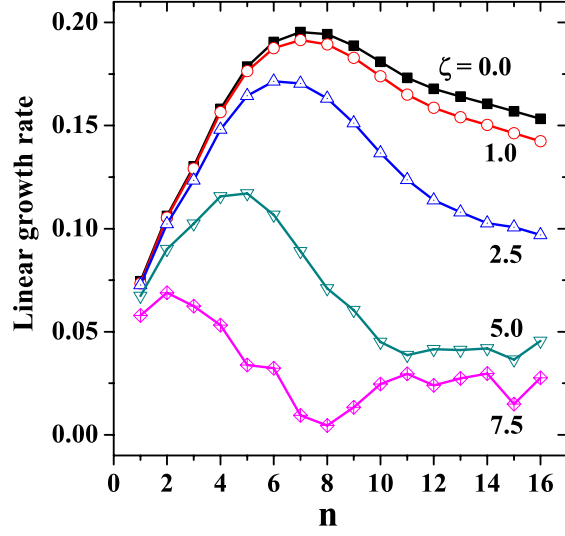


Figure 4.4: The ζ dependence of the linear growth rate for each toroidal Fourier mode number n .

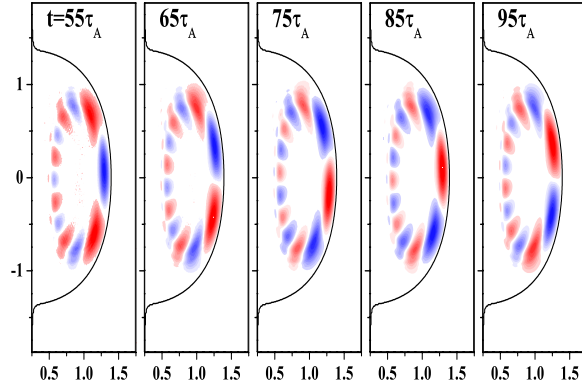


Figure 4.5: Time development of the poloidal mode structures. An image contour map for the $n = 5$ component of the pressure is indicated in each panel using $\zeta = 5.0$.

direction with almost the same rotation speed as the local poloidal diamagnetic drift velocity which is indicated by Fig. 4.1(b). Since the rotational flow shear has comparable spatial and temporal scale to the growing mode components, the mode structures are gradually distorted and the excited energy is dissipated within the time scale of the linear growth. This might be the basic mechanism for the suppression of the mode growth due to the global flow shear. The distortion would be more effective for smaller wavelength components than larger ones, if one assumes that the mode structures extend closely to each other mode. Thus, the higher- n components are suppressed, and the linear growths are dominated by the lower- n components for finite ζ cases.

4.2 Formation of filamentary structure

In the drift model simulation, the hyper harmonics of the dominant modes are also excited as well as the MHD case, when the amplitude of the instability becomes large. One can see the excitation of such hyper harmonics in Fig. 4.2(a,b), where the $n = 12$ modes induced as the hyper harmonics of the $n = 6$ mode abruptly change their growth rate at $t = 45\tau_A$ for $\zeta = 1.0$ and at $t = 60\tau_A$ for $\zeta = 2.5$. Similarly in Fig. 4.3(a) $n = 9$ mode is also excited at $t = 85\tau_A$ by the coupling of $n = 5$ and 4 for $\zeta = 5.0$, and in (b) $n = 4$ and 6 modes induced as hyper harmonics of $n = 2$ at $t = 150\tau_A$ for $\zeta = 7.5$. Such excitation results in nonlinear growth of the high- n modes, later steepening of pressure gradient in the edge region during

the formation of balloons or finger in the outer edge region. Such localization along the plasma pressure iso-surface can be clearly seen in the Fig. 4.6 for (a) $\zeta = 1.0$ at $t = 80\tau_A$, (b) $\zeta = 5.0$ at $t = 130\tau_A$ and (c) $\zeta = 7.5$ at $t = 225\tau_A$. These times represents the time of the middle of the ELM rise for different ζ cases. If we compare this with the MHD case (*i.e.*, Fig.3.5(b) at $t = 70\tau_A$), we will see lot of similarities. The ejection process of the balloons can be clearly seen. The balloons are formed in helically twisted shapes along the magnetic field. The formation of balloons looks similar with the only difference in the number of ridges or fingers on the plasma pressure iso-surface. It is because of the difference in the dominant linear toroidal mode number (*i.e.* precursor) preceding the nonlinear phase (e.g. for case (a) $n = 9$, (b) $n = 5$ and for (c) $n = 2$ are the dominant precursors). Once the highly nonlinear phase is achieved, some of the balloons are separated from the core plasma and ejected into the open field region. The three pairs of panels of Fig. 4.7 and 4.8 show the formation of filamentary structures for different ζ cases. It should be noted that for all cases clear filaments are erupts on the plasma surface and separated from the core. It shows similarities with the non-uniform growth of filament because of the coupling of toroidal modes. So even with the rotation of the toroidal modes, coupling is still effective, and that results in fewer filaments then the dominant toroidal mode number. Also, irrespective of the suppression of the intermediate toroidal modes in linear phase the overall behavior of the modes structure in nonlinear phase are similar

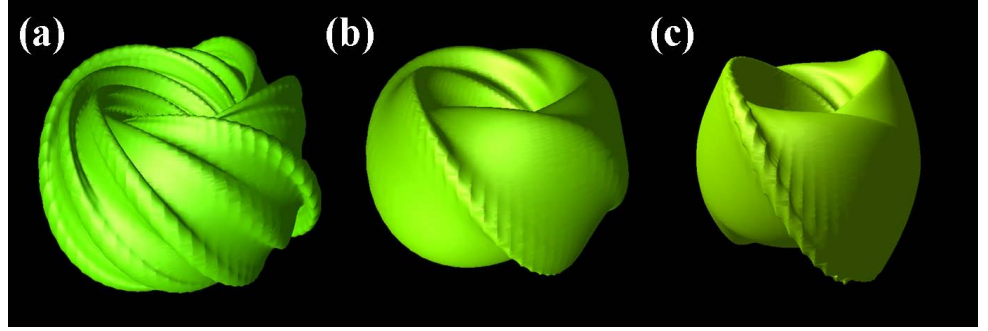


Figure 4.6: A localized formation of balloon also called as finger structure at (a) $t = 80\tau_A$, $\zeta = 1.0$, (b) $t = 130\tau_A$, $\zeta = 5.0$, and (c) $t = 225\tau_A$, $\zeta = 7.5$. It is shown in a bird's-eye view of the iso-pressure surface with the time near the middle of onset of ELM.

to MHD model where the high modes are the fastest growing modes and saturates with the formation of filaments.

4.3 Field line behavior

Field line behavior is very important in investigation of formation of filamentary structure as already discussed in MHD simulation in section (3.3.3). In this section we will investigate the behavior of magnetic field as well as the behavior of stream lines with the introduction of FLR effect. Figure 4.9 shows the plasma pressure iso-contour (green), arbitrary traces of magnetic field lines (blue) and the stream lines (red) for $\zeta = 1.0$, 5.0 and 7.5 in the early nonlinear phase. The deformations into balloons along the magnetic field lines in the outer edge region can be formed in these three different cases. However if we closely look at the behavior of stream lines, it looks much different then the MHD case. For low value of ζ as shown in

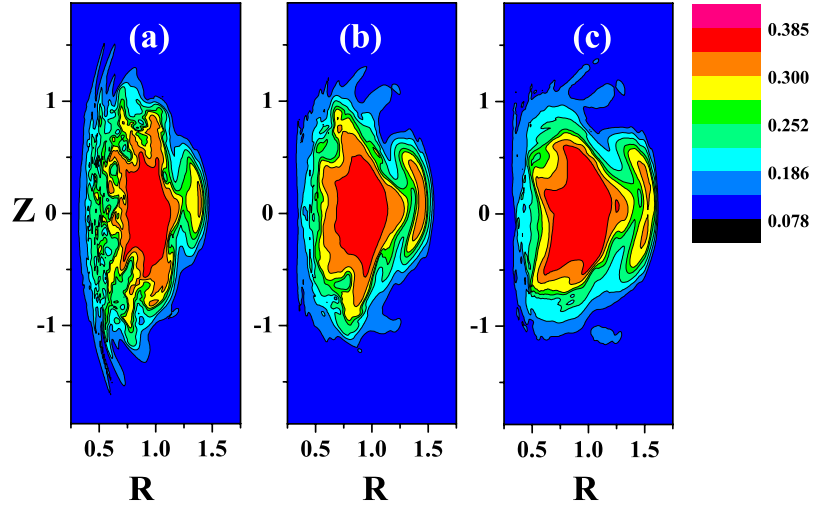


Figure 4.7: Formation of filamentary structure shown in the image contour map of the poloidal pressure profiles in a poloidal cross section. Time and the ζ are (a) $t = 90\tau_A$, $\zeta = 1.0$, (b) $t = 145\tau_A$, $\zeta = 5.0$, and (c) $t = 235\tau_A$, $\zeta = 7.5$.

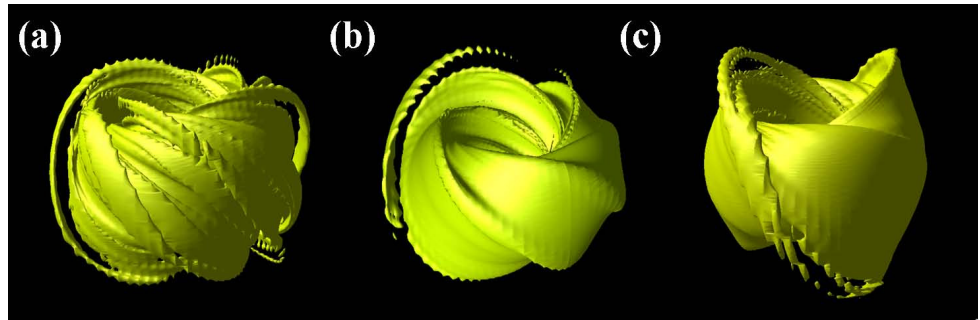


Figure 4.8: Formation of filamentary structure shown in a bird's-eye view of the iso-pressure surface at (a) $t = 90\tau_A$, $\zeta = 1.0$, (b) $t = 145\tau_A$, $\zeta = 5.0$, and (c) $t = 235\tau_A$, $\zeta = 7.5$. This stage can also be related to the time near the end of ELM rise.

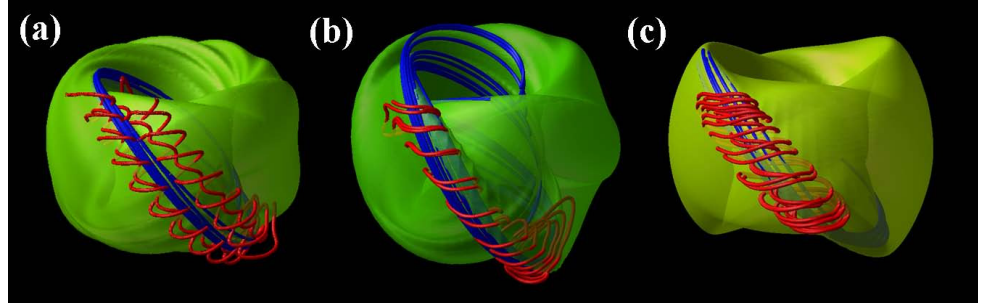


Figure 4.9: Three dimensional geometry containing plasma pressure iso-contour (green), arbitrary traces of magnetic field line (blue), and the stream line (red) using (a) $\zeta = 1.0$ at $t = 70\tau_A$, (b) $\zeta = 5.0$ at $t = 130\tau_A$ and (c) $\zeta = 7.5$ at $t = 220\tau_A$. For small ζ value the flow pattern is not modified, but with intermediate and high FLR correction there is a change in flow pattern from twin to single vortex structure.

Fig.4.9(a) we observe twin vortex flow pattern which is quite similar to the MHD case. However if we raise the value of ζ to intermediate and high level as shown in 4.9(b,c), the twin vortex convective rolls of MHD case are no longer apparent. Instead because of diamagnetic drift represented by (2.12) vortex has formed in the direction encircling each balloon and convecting across the radial direction. Reflecting such diamagnetic drift flows, the plasma flow structure then turns into a single-vortex one on the balloon, as shown in Fig. 4.10.

If we compare the local flow speed with the radial velocity of the filament in outward direction. We found that local flow speed for the vortices is 20 times larger than the eruption of filaments for each case. Therefore, the formation mechanism of the filamentary structure and its separation from the core seem not to be related to the vortex motion at the balloons. Thus, the dynamics for the eruption of filament can be considered to be determined mostly by the MHD terms.

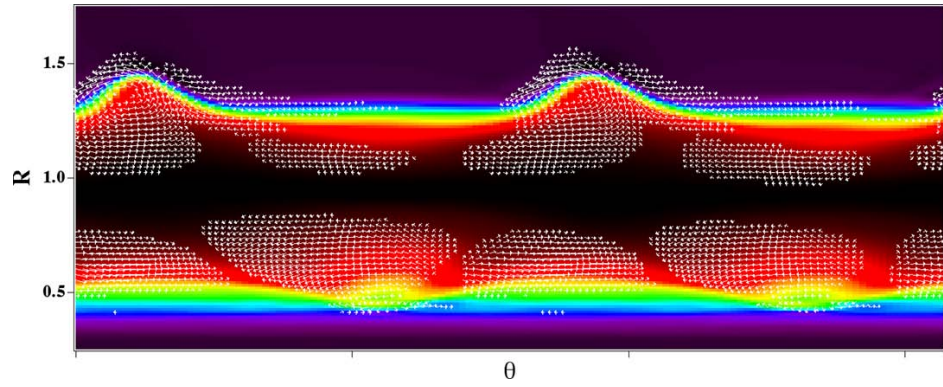


Figure 4.10: Toroidal flow pattern on the equatorial plane for the $\zeta = 7.5$ case at $t = 190\tau_A$. The plasma toroidal flow velocity is represented by fine arrows. The color contour map indicates the plasma pressure, where the color varies from blue, green, red, to black as the pressure increases.

Chapter 5

Discussion

5.1 Comparison with observation

In this section, we will compare our simulation results with the experimental observation of the evolution of filament structures during ELMs. As described earlier in Chapter 1, the evidence of the spatial localization of ELM structure come from a variety of tokamak and experimental techniques. For example, COMPASS-D, JET, ASDEX Upgrade, NSTX and MAST. But in current study our main focus is on ELMs observed at ST like MAST and NSTX. As mentioned earlier, measurement of spatial and temporal structure of ELM in MAST provides strong evidence for the ELM to be a filament-like structure which have ballooning nature. These structure erupts from outboard side with a typical time scale of $\sim 100\mu\text{ sec}$ [1]. The structure are elongated along the magnetic field lines with a toroidal mode number between 8 and 12 but localized about it[2]. The onset of Type I ELMs can be thought to be related to the ballooning mode[2] since they are triggered near the ballooning stability limit. In fact, the MHD fluctuations are observed as the precursor preceding the crash phase, both the intermediate- n ($n = 5 - 12$) precursors and the low- n ($n = 1 - 2$) deformations are observed in the experiments[2, 34]. Evidence of reconnection has also been

observed near the end of ELM rise from the D_α signal and the magnetic fluctuation signal[3].

5.1.1 The mode structure of ELMs

Our nonlinear simulations are executed in a three dimensional full toroidal geometry. The initial MHD equilibrium for the simulation is calculated through Grad-Shafranov equations. The profiles are selected to be moderately broad in the core region following the conventional experiments. During the linear analysis, the intermediate- n modes are linearly unstable with larger growth rates as shown in Fig.5.2. The high- n and low- n modes are nonlinearly driven as the intermediate- n modes acquires finite amplitude. And hence the nonlinear phase is dependent on these intermediate modes precursors.

Experimentally, it has been observed in a number of machines, especially on MAST that the ELMs have a typical filamentary structure with a toroidal mode number ~ 10 . The toroidal mode number of these filament has been extracted from a study of discrete peak observed in the ion saturation current recorded by a mid-plane reciprocating probe[3]. Interpreting the J_{SAT} peak as a filament rotating with the plasma past the probe, the toroidal mode number can be derived using,

$$\text{mode number} = 2\pi \frac{R_{outer}}{V_{ped}\Delta t} \quad (5.1)$$

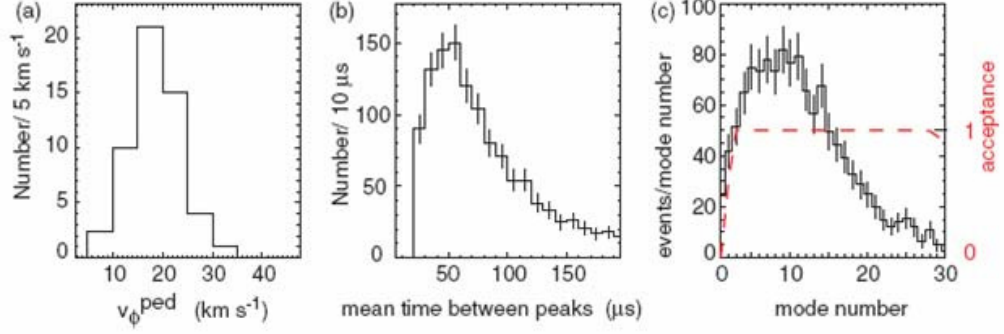


Figure 5.1: (a) The distribution of the V_{ped} from CXRS. (b) The distribution of the mean per ELM time difference between peaks in the ion saturation current observed by the mid-plane reciprocating probe. (c) The distribution of derived mode number (the dashed curve shows the results of a simulation of the spectral acceptance) [3].

where R_{outer} is the radius of the plasma at the outboard LCFS, V_{ped} is the toroidal velocity of the plasma at the top of the pedestal as shown in Fig.5.1(a), and Δt is the time difference between the peaks in the ion flux (J_{SAT}) observed at reciprocating probe for each ELM as shown in Fig.5.1(b). The distribution has a mean of $75\mu\text{sec}$, and the majority of peaks have a mean time separation of $< 100\mu\text{sec}$. The toroidal mode number is estimated from the distribution as shown in Fig.5.1(c) with the peak value at $n = 10$ and mean is 11. If we compare this with our simulation as shown in Fig.5.2, it shows the dominance of intermediate eigen modes *i.e.*, ($n = 5 - 11$) with the peak value at $n = 8$ and 9. Hence our simulation agrees with this characteristic of Type I ELM.

If we look further at the behavior of these modes, we found that these intermediate modes are ideal modes with ballooning nature. Figure 3.2(a) shows the poloidal cross-section of the fluctuation component in the pressure for the dominant toroidal

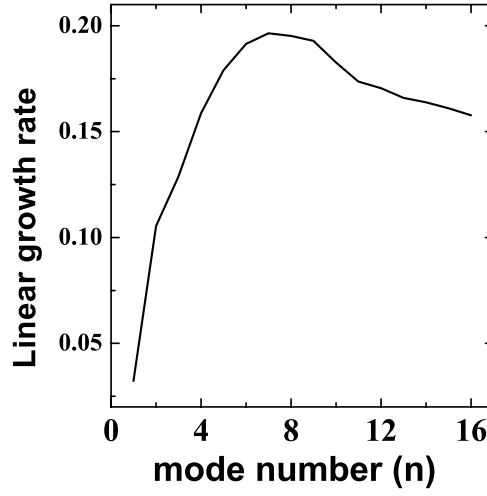


Figure 5.2: Growth rate of the linear eigen modes for MHD simulation.

mode (*i.e.*, $n = 9$). It shows clearly that these modes are poloidally localized in the so-called bad-curvature region with unstable mode peaks in the outboard side of plasma. Similarly, Fig. 3.2(b) shows the poloidal Fourier expansion of the magnetic field energy, identifying the superposition of multiple poloidal components. Both of these figures supports the ballooning nature of these intermediate modes. Similar results were observed for Type I ELM in MAST[2] and in ASDEX Upgrade experiments[32], where they appear to be associated with a line of approximately constant pedestal pressure, often in the vicinity of the ballooning stability boundary. Thomson scattering profiles obtained during these ELMs [2] showed the formation of a broad tail in both the density and the temperature profiles at the outboard mid-plane

but no change on the inboard side, which is consistent with the ballooning nature of ELMs.

5.1.2 The spatial structure of ELMs

The evidence of spatial structure has come from a variety of tokamaks and experimental techniques. Because of excellent diagnostic visibility, remote first wall and extensive divertor and edge diagnostic makes MAST an ideal device for the study of ELMs. One of the most prominent features on the ELM crash is the emergence of the filamentary structure[1, 2, 3] as shown in Fig. 1.8 and 1.9. The camera images of the visible lights show several numbers of helically twisted bright stripes on the plasma surface. Some of them are raised and separated from the core, forming an arcade into the scrape-off layer region. In order to extract information on the spatial structure of ELMs from Fig. 1.8, we performed the MHD simulation. Our simulation shows clearly the emergence of fingers or balloons on the three dimensional pressure surface which later results in separation of filamentary structure. These behaviors well agree with experimental observation of shot #8814 (*i.e.*, Fig. 1.8). Especially, Fig. 3.5 shows quite similar behavior to the MAST observation.

Further evidence for the time evolution of the ELM filament comes from the data shot #14648 of the new multi-time point edge Nd-YAG Thomson scattering system on MAST[81]. Figure 5.3(a) and (b) show the edge density and temperature profiles of a case where a filament is in the line of sight of the diagnostic. The tim-

ing of the laser pulses relative to the target D_α light is shown in Fig. 5.3(c); they are separated by $5\mu\text{sec}$ starting $53\mu\text{sec}$ after the start of the ELM. The first density profile (red open circles) in Fig. 5.3 shows the formation of an outboard tail. The second density profile is obtained $5\mu\text{sec}$ later, shows the radial expansion of the density perturbation. The third density profile (open blue triangles) shows a sudden change in the profile; the filament has detached from the LCFS leaving a depression behind in the density profile. The electron temperature in this detached filament remains around 80eV . The characteristic of ELM observed in this figure is reproduced through our simulation result as shown in Fig. 5.4(a). Using the parameters of the MAST experiment, the normalization of the time scales for the current shot is estimated as $1(\tau_A) \sim 0.47(\mu\text{sec})$. With this conversion we can compare simulation time scale with the real experiment. At time $t = 50\tau_A$, which is the earlier nonlinear phase we observed a steep pressure gradient in the core region, which become steeper at later time, (*i.e.*, $t = 60\tau_A$) because of the excitation of high ballooning mode number. The behavior of pressure profile is similar to the first density profile observed in experiment, and hence can be named as the time of the onset of ELMs. At $t = 70\tau_A$ the the pressure profile shows the formation of small hump on the edge pedestal because of the radial expansion of pressure perturbation. The difference of time between the onset of ELM and near the middle of ELM is about $5\mu\text{sec}$ (*i.e.*, $10\tau_A$) with radial expansion of about 1.5cm , which is similar to the second density profile. Once the time reaches $80\tau_A$ (*i.e.* $5\mu\text{sec}$ later), we found a small peak of pressure in SOL region

leaving depression behind the pressure profile similar to the third density profile of Fig. 5.3[81].

Figure 5.4(b) shows the overall time evolution of radial pressure profile starting from linear phase till the burst of ELM. It shows clearly the steepening of pressure gradient in the early nonlinear phase and then resulting in eruption of filament from the edge pedestal. It clearly shows the convective nature of plasma loss, which is also in agreement with the experimental observation[2].

As for the time scale, the total scenario for the ELM crash ends within almost $100\tau_A$, which corresponds to several tens of microseconds with our normalization. This time scale agrees with that of the experimental ELM crash time scale[2]. It should be also noted that such outstanding filament can be experimentally observed only in a few direction[1], corresponding to our simulation result. This happens because of the nonlinear coupling of the toroidal mode number. We showed in Fig. 3.6(b), the possible alignments of the dominant toroidal mode number $n = 9$ and 5, resulting in non-uniform growth of filaments.

We also showed that these filamentary structure is correspondent to the convection motion of the plasma flows, which forms a twin-vortex flow pattern in such a way that the plasma moves in outward direction, pushing the core plasma from inside to outside of the torus (see Fig. 3.8). When the balloon structure is initially formed at the plasma surface, the magnetic field lines on both sides of the separatrix are pushed against each other by such perpendicular flows due to the spouting-out and

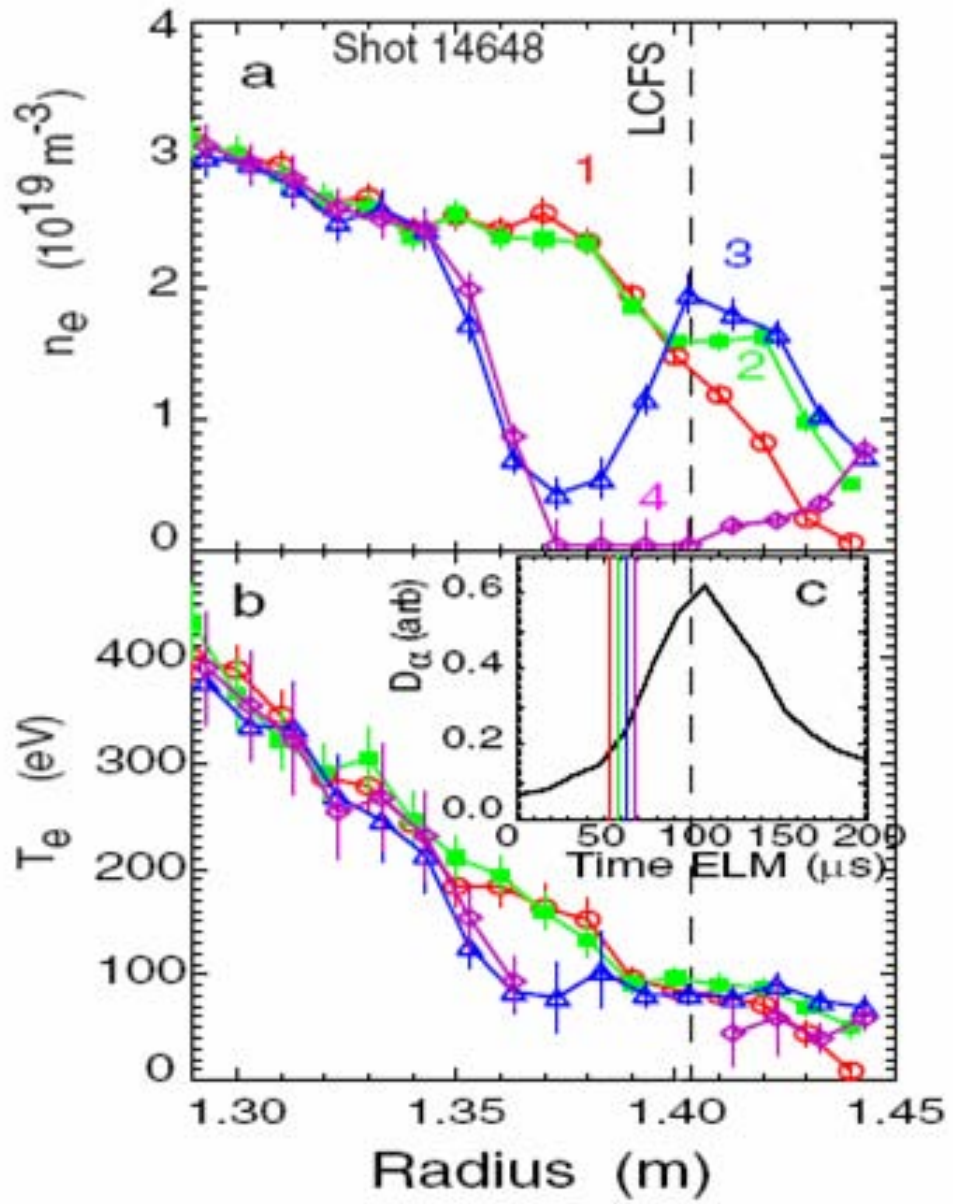


Figure 5.3: The time evolution of (a) the edge density profile and (b) the edge temperature profile for single ELM. (c) The target signal as a function of time [81].

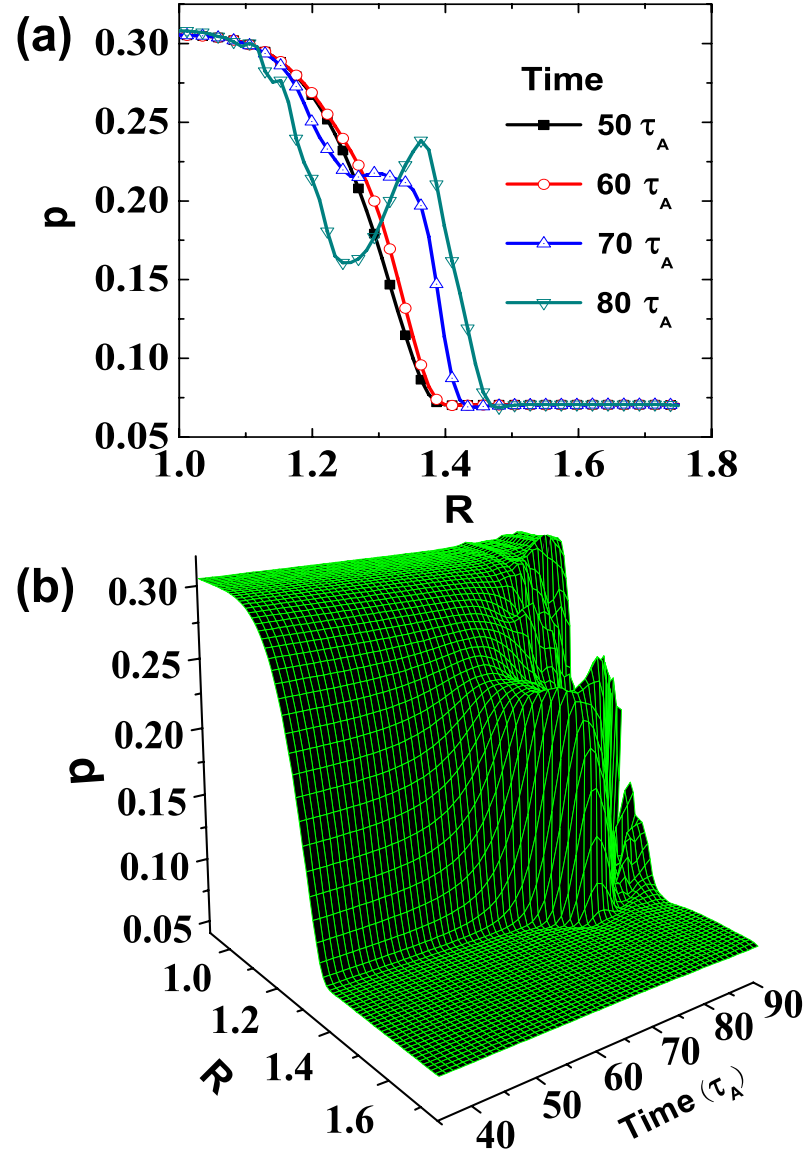


Figure 5.4: Time evolution of edge pressure profile along major radius R . (a) Radial pressure profile at $t = 50\tau_A$ (early nonlinear phase), $t = 60\tau_A$ (at the time of onset of ELM), $t = 70\tau_A$ (in the middle of ELM rise) and $t = 80\tau_A$ (near the end of ELM rise). (b) Radial time evolution of pressure profile from linear till the end of nonlinear phase.

the perfect conductor conserving the poloidal flux. Under this situation, the reconnection of the field lines can effectively occur by the driven reconnection mechanism. Once such reconnection occurs as shown in Fig. 3.9(c) at $t = 82\tau_A$, the plasma rapidly flows out through the reconnected field lines due to the parallel pressure gradient, leading to the filamentary structure. After the internal free energy is partially lost by such convective processes, the system ceases to develop and reaches a relaxed state. If we investigate the experimental observation, possible evidence of reconnection comes from the fast magnetics installed on MAST (see Fig. 11 of Ref.[3]). It shows the magnetic fluctuation signal during an ELM. There is a very brief ($\sim 5\mu\text{sec}$) event just before the peak in the $D\alpha$ signal, which occurs at the time similar to the predicted reconnection event (*i.e.*, near the end of ELM rise). After the reconnection it is not known experimentally, whether or not the filament remains attached to the core at some location away from the outboard mid-plane. However, our simulation shows that the filament disappears after the reconnection as shown in Fig. 3.9(c) at $t = 82\tau_A$.

5.2 Comparison with theory

Our simulation results are also consistent with the prediction of the theoretical models related to the early nonlinear ballooning modes in the geometry of tokamak[43, 64]. According to them, during the nonlinear evolution of the ballooning mode, the plasma develops filamentary structure that are elongated along the field line. On the

outboard side of the tokamak plasma, the filaments are displaced radially a large distance from the field line on which they originated. However on the inboard side the displacement is much more less. If we compare the above prediction with our simulation, Fig. 3.5 shows clearly the formation of filamentary structure during the nonlinear evolution of ballooning mode. Also in Fig. 3.7, we showed that these filamentary structure are elongated along the magnetic field line and are displayed radially a large distance from the field line on which they were generated.

In our simulation, after such a nonlinear development, considerable amount of plasma can be lost out of the separatrix by purely dynamical processes. Since no microscopic transport mechanism is included here, therefore we cannot estimate the amount of heat and particle lost from the filamentary structure. These results are compared qualitatively with the experimental observation of the ELMs in MAST and NSTX experiments. Good agreement is found in the following characteristics formation of filaments separating from the core, non-uniform growth of filaments due to toroidal mode coupling, time scale of ELM crash, triggering by the ideal ballooning mode, presence of intermediate- n precursors and loss of plasma through convective process. Thus, our simulation result well reproduces the experimental observations of the ELM crash in ST. Therefore, it can be considered that our simulation roughly follows the experimental situation at the onset of the ELM crash phase.[84, 86, 87]

5.3 Effect of FLR correction

The evolution of ballooning mode instability has been studied using finite Larmor radius correction in MHD theory. Figure 4.1 shows the toroidal as well as poloidal flow component of ion diamagnetic drift velocity. It shows a localized strong shear in the edge region. Such diamagnetic flow have a stabilizing influence on the unstable ballooning modes. It was shown by Cooper [82] that the flow shear changes the time behavior of the ballooning instability from purely exponentially growing mode to an instability with phases of fast growth alternating with period of slow growth or decay. Hence the net growth rate is reduced by flow shear. And that can be seen in the Fig. 4.4, where the net growth rate is reduced with the increase in value of ζ (*i.e.* diamagnetic flow). As shown in Fig. 4.4, for $\zeta = 1.0$, we observed clear suppression in the growth of high mode number as compare to intermediate modes. When the value of ζ is raised to higher exaggerated values, we see significant change in the growth rate of the high and intermediate mode. The reason for low ζ to be less effective in the stabilization of intermediate mode is because of the radial variation of ω_{dia} [69], when ζ is weak, a small increase in the pressure gradient allows $\gamma_{MHD} > \frac{\omega_{dia}}{2}$ [83] to be satisfied and the strong MHD can grow. However with higher value ζ (*i.e.*, 2.5, 5.0, 7.5), large pressure gradient are needed to satisfy the above equation, and so they are diamagnetically suppressed mode, giving rise to smaller ELMs having reduced growth rates. If we compare the linear phase of both the MHD and drift simulation result, we found that the FLR-MHD clearly grows slower than the MHD, the

higher modes do not grow linearly, in contrast to MHD simulation where intermediate modes appear to be the dominant one. Hence we found effective stabilization of higher modes for weak ζ , and intermediate modes for higher value of ζ .

In the nonlinear phase, irrespective of the suppression of the intermediate toroidal modes in linear phase the overall behavior of the modes structure as shown in Fig. 4.2 and 4.3 looks similar to MHD model simulation (see Fig. 3.1) where the high modes are the fastest growing modes and saturates with the formation of filaments. If we compare the formation of filamentary structure as shown in Fig. 4.8 with the MHD model, we observed similar eruption of filaments, that are localized along the field line in toroidal as well as poloidal direction. The field line behavior also looks similar to the MHD simulation, with the exception of flow pattern of stream line for high ζ , where the plasma flow structure turns into a single vortex on the balloon structure. This looks very interesting and need to be explore in future studies. The important similarity between the MHD, and the FLR simulation with the experimental observation is the existence of the filamentary structure. One more similarity that need to mention here is the eruption of fewer number of filament as compare to the dominant mode number, which shows that even with the toroidal and poloidal rotation of the perturbation, the modes are aligned along the position of the eruption of filaments, giving rise to nonuniform growth of filament which also looks an interesting result.

[85, 84]

Chapter 6

Concluding remarks

6.1 Summary

Numerical simulations based on the MHD and the drift models have been executed for the purpose of revealing the nonlinear dynamics of the ballooning mode in toroidal plasma. The simulation starts from linearly unstable configuration which causes initial tiny perturbation introduced on the plasma velocity field to grow spontaneously with a specific eigen function. During linear analysis, the intermediate- n modes (*i.e.*, $n = 5 - 10$) have larger growth rates than others. These intermediate- n modes have a ballooning mode nature, the mode structures are poloidally localized in the bad curvature region, and have a wide envelope consisting of several poloidal components. As for the effect of resistivity, there is no significant change in the growth rate for $\eta \leq 1 \times 10^{-5}$. Therefore, it can be identified that these modes are mainly ideal in nature for those parameter ranges. In the nonlinear phase, the MHD ballooning modes evolve into a nonlinear structure that result in the formation of a number of hot plasma filaments, elongated along a magnetic field line, but localized about it. These filaments extend out into the scrape-off layer on the outboard side but remain connected back into the pedestal region on the inboard side. This filamentary structure is correspondent to the convection motion of the plasma flows, which forms a

twin-vortex flow pattern in such a way that the plasma moves in outward direction, pushing the core plasma from inside to outside of the torus. When the balloon structure is initially formed at the plasma surface, the magnetic field lines on both sides of the separatrix are pushed against each other by such perpendicular flows due to the spouting-out and the perfect conductor conserving the poloidal flux. Under this situation, the reconnection of the field lines can effectively occur by the driven reconnection mechanism. Once such reconnection occurs, the plasma rapidly flows out through the reconnected field lines due to the parallel pressure gradient, leading to the filamentary structure. After the internal free energy is partially lost by such convective processes, the system ceases to develop and reaches a relaxed state.

The simulation results corresponding to the ELM crash phase in ST plasma have reproduced the experimental observations qualitatively. These results were compared with the Type I ELM observed in MAST[1, 2, 3], and NSTX[33, 34]. Qualitatively, good agreement is found in the following characteristic of Type I ELM:

- Triggered by the ideal ballooning mode
- Presence of intermediate- n precursors preceding the crash
- Emergence of filamentary structure during the onset of ELM
- Non uniform growth of filament, resulting from the nonlinear toroidal mode coupling
- Convective loss of plasma from the edge pedestal during the onset of ELM

- Time scale of ELM crash.

Moreover, the simplified drift model, where the ion diamagnetic drift effect is included in the advection term of the equation of motion, has been applied to the linear and nonlinear simulations. This modification has been found to suppress the higher- n components linearly, since the mode growth is suppressed by the sheared toroidal and poloidal flows. We also found that although the linear phase is substantially modified with the introduction of FLR effect, however in the nonlinear phase all the above discussion of MHD simulation are fully applicable with the exception of the formation of single vortex flow pattern for higher ζ value.

6.2 Future directions

First among other questions for future investigation is the identification of the discrepancy between the nonlinear phase of both the MHD and the drift model simulation. Though there is a similarity in the formation and separation of filamentary structure in both the model, but still there is difference in the flow pattern of the stream lines. Therefore, further work is necessary to pinpoint the reasons for the discrepancy in the flow pattern for the two models. One of the reason behind such contrast in flow pattern comes from the inclusion of only the advection term of \mathbf{v}_p in momentum equation, and ignoring the rest of the correction that comes with drift model. We need to include the rest of the terms also for the drift model.

The bootstrap current has been found to play important role in edge stability in the literature. Its inclusion has been found to be essential in order for calculated kink-peeling/ballooning stability boundaries to agree with experiment. Hence, in order to study the coupling of ballooning-peeling mode, which have been observed in number of devices the inclusion of bootstrap current can be helpful.

The qualitative nonlinear behaviors discovered through our simulation are very much in agreement with the experimental observation of MAST. Therefore another direction for future work is to investigate the ELMs on other devices like conventional tokamak geometry, and the Large Helical Device (LHD) geometry etc. It would be an interesting study to compare the simulation results of ELMs using various kind of toroidal geometries.

Bibliography

- [1] A. Kirk *et al.*, *Spatial and Temporal Structure of Edge-Localized Modes*, Phys. Rev. Lett. **92**, 245002-4 (2004).
- [2] A. Kirk *et al.*, *ELM characteristics in MAST*, Plasma Physics and Controlled Fusion **46**, 551 (2004).
- [3] A. Kirk *et al.*, *Structure of ELMs in MAST and the implications for energy deposition*, Plasma Physics and Controlled Fusion **47**, 315-333 (2005).
- [4] B. Coppi and M. N. Rosenbluth, *Collisional interchange instabilities in shear and $\int (dl) / B$ stabilized systems*. In IAEA Culham, 617 (1965).
- [5] J. W. Connor, R. J. Hastie, and J. B. Taylor, *Shear, Periodicity and, Plasma Ballooning Modes*, Phys. Rev. Lett. **40**, 396 (1978).
- [6] H. P. Furth, J. Killeen, M. N. Rosenbluth, and B. Coppi, Plasma Physics and controlled nuclear fusion research 1964, IAEA, Vienna, **1**, 103 (1965).
- [7] J. M. Greene and J. L. Johnson, *Interchange instabilities in ideal hydromagnetic theory*, Plasma Physics, (Pergamon Press, Northern Ireland), **10**, 729-745 (1968).
- [8] J. Wesson, *Tokamaks*. Oxford Engineering Science. (Oxford University Press, 3rd edition, 2004).
- [9] J. M. Greene, and M. S. Chance, *The second region of stability against ballooning modes*, Nucl. Fusion **21** 453 (1981).
- [10] R. L. Miller, Y. R. Lin-Liu, , T. H. Osborne, and T. S. Taylor, *Ballooning mode stability for self-consistent pressure and current profiles at the H-mode edge*, Plasma Physics and Controlled Fusion **40** 753 (1998).
- [11] F. Wagner *et al.*, *Regime of improved confinement and high beta in neutral-beam heated divertor discharges of the ASDEX tokamak*, Phys. Rev. Lett. **49**, 1408 (1982).

- [12] T. Fujita. *Spatial structure of internal and edge transport barriers*. Plasma Physics and Controlled Fusion, **44**(Supplement 5A) A19-35 (2001).
- [13] F Wagner *et al.*, *Recent results of H-mode studies on ASDEX*. In 13th International Conference of Plasma physics and controlled nuclear fusion (IAEA Vienna), **1**, 277-290 (1990).
- [14] R J Groebner and T H Osbourne, *Scaling studies of high mode pedestal*. Physics of Plasmas, **5**, 1800-1806 (1998).
- [15] H. Zohm, *Edge localized modes (ELMs)*. Plasma Physics and Controlled Fusion, **38**, 105 (1996).
- [16] J. W. Connor, *Edge-localized modes-physics and theory*, Plasma Physics and Controlled Fusion, **40**, 531 (1998).
- [17] J. W. Connor, R. J. Hastie, and H. R. Wilson, *Magnetohydrodynamic stability of tokamak edge plasmas*. Physics of Plasmas, **5**, 2687 (1998).
- [18] E. J. Doyle *et al.*, *Modifications in turbulence and edge electric fields at the L-H transition in the DIII-D tokamak*, Phys. Fluids B **3**, 2300 (1991).
- [19] P. Gohil *et al.*, *Study of giant edge-localized modes in DIII-D and comparison with ballooning theory*. Physical Review Letters, **61**, 1603-06 (1988).
- [20] J. Lingertat *et al.*, *The ELM operational window and power deposition in JET*. In 24th EPS Conference on Controlled Fusion and Plasma Physics, Poster 24 (1997).
- [21] T. Kass, S. Gunter, M. Marascheck, W. Suttrop, H. Zohm, and the ASDEX-Upgrade team., *Characteristics of Type I and Type III ELM Precursors in ASDEX Upgrade*, Nuclear Fusion, **38**, 111 (1998).
- [22] Y. Kamada, K. Ushigusa, O. Naito, S. Ishida, T. Fujita, R. Yoshino, M. Kikuchi, M. Mori, and H. Ninomiya. *ELMy H-mode with high N and high p in JT-60U*. Plasma Physics and Controlled Fusion, **36**, A123-A128 (1994).
- [23] R. Maingi *et al.*, *ELMs and the H-mode pedestal in NSTX*. J. Nucl. Mater. **337-339** 727 (2005)
- [24] P. B. Snyder *et al.*, *Edge localized modes and the pedestal: A model based on coupled peeling-ballooning modes*. Physics of Plasma, **5**, 2037-43 (2002).

- [25] P. B. Snyder *et al.*, *Progress in the peeling-ballooning model of edge localized modes: Numerical Studies of nonlinear dynamics*. Physics of Plasma, **12**, 056115 (2005).
- [26] T Ozeki *et al.*, *Plasma shaping, edge ballooning stability and ELM behaviour in DIII-D*. Nuclear Fusion, **30**, 1425 (1990).
- [27] S. Fielding *et al.*, *The H-mode in COMPASS-D*. Plasma Physics and Controlled Nuclear Fusion, **38**, 1091-1102 (1996).
- [28] K. H. Burrell *et al.*, *Quiescent H-mode plasmas in the DIII-D tokamak*, Plasma Phys. and Contr. Fusion, **44**, A253 (2002).
- [29] W. Suttrop *et al.*, *ELM-free stationary H-mode plasmas in the ASDEX Upgrade tokamak*, Plasma Physics and Controlled Fusion **45**, 1399 (2003).
- [30] Y. Takase *et al.*, *Radiofrequency-heated enhanced confinement modes in the Alcator C-Mod tokamak*, Phys. of Plasmas **4**, 1647 (1997).
- [31] A. E. Hubbard *et al.*, *Pedestal profiles and fluctuations in C-Mod enhanced D-alpha H-modes*, Phys. of Plasmas **8**, 2033 (2001).
- [32] W. Suttrop *et al.*, *Identification of plasma-edge-related operational regime boundaries and the effect of edge instability on confinement in ASDEX Upgrade*, Plasma Phys. and Contr. Fusion **39**, 2051 (1997).
- [33] R. Maingi *et al.*, *Observation of a high performance operating regime with small edge-localized modes in the National Spherical Torus Experiment*. Nucl. Fusion **45**, 264–270 (2005)
- [34] R. Maingi *et al.*, *H-mode turbulence, power threshold, ELM, and pedestal studies in NSTX*. PPPL-4016 (2004).
- [35] M. Marascheck *et al.*, *MHD Characteristics of ELMs and their Precursors*”, Proceedings of 25th EPS Conference on Controlled Fusion, Prague, 492 (1998).
- [36] T. Bolzonella *et al.*, *ELM-related High Frequency MHD Activity in ASDEX Upgrade*, 29th EPS Conference on Plasma Phys. Contr. Fusion, (Montreaux) Vol. 26B, P-1. 038 (2002).

- [37] J. W. Connor *A review of models for ELMs*, Plasma Phys. and Contr. Fusion, **40**, 191 (1998).
- [38] C. P. Perez *et al.*, *Type-I ELM Precursor Modes in JET*, Nucl. Fusion **44**, 609–623 (2004).
- [39] C. P. Perez *et al.*, *Washboard modes as ELM-related events in JET*, Plasma Phys. and Contr. Fusion **46**, 61 (2004).
- [40] The JET Team, *The Route to High Performance on JET*, Plasma Physics and Controlled Fusion **37** A359 (1995).
- [41] A. W. Leonard *et al.*, *Impact of ELMs on the ITER divertor*, J. Nucl Mater. **109**, 266–269 (1999).
- [42] F. Wagner *et al.*, *H-mode of W7-AS Stellarator*, Plasma Physics and Controlled Fusion **36** A61 (1994).
- [43] S. C. Cowley, H. Wilson, O. Hurricane, B. Fong, *Explosive instabilities: from solar flares to edge localized modes in tokamaks*, Plasma Physics and Controlled Fusion **45**, A31 (2003).
- [44] Y-K. M. Peng *et al.*, *Features of Spherical Torus Plasmas*, Nucl. Fusion **26**, 769–777 (1986).
- [45] A. Sykes *et al.*, *H-Mode operation in the START spherical tokamak*, Phys. Rev. Lett. **84**, 495 (2000).
- [46] C. M. Roach, R. J. Akers, N. J. Conway, T. M. Dodge, M. P. Gryaznevich, P. Helander, A. Sykes, M. J. Walsh, START Team, NBI Team. *Confinement in START beam heated discharges*, Nucl. Fusion **41**, 11–30 (2001).
- [47] M. Gryaznevich *et al.*, *Achievement of record β in the START spherical tokamak*, Phys. Rev. Lett. **80**, 3972 (1998).
- [48] A. C. Darke *et al.*, Proc. 18th Symp. on Fusion Technology (Karlsruhe, Germany, 22–26 August 1994) vol 1 (Amsterdam: Elsevier) 799 (1995).
- [49] M. Ono *et al.*, Proc. 18th IAEA Fusion Energy Conf. (Sorrento) Paper EX7/5 (2000).

- [50] F. Troyon, R. Gruber, H. Saurenmann, S. Semenzato, and S. Succi, *MHD-limits to plasma confinement*, Plasma Physics and Controlled Fusion **26**, 209 (1984).
- [51] T. C. Hender *et al.*, *Magneto-hydrodynamic limits in spherical tokamaks*, Physics of Plasmas **6**, 1958 (1999).
- [52] R. J. Bickerton, J. W. Connor, and J. B. Taylor, *Diffusion driven plasma currents and bootstrap tokamak*, Nature Physical Science **229**, 110 (1971).
- [53] H. R. Wilson *et al.*, *Integrated plasma physics modelling for the culham steady state spherical tokamak fusion power plant*, Nuclear Fusion **44**, 917 (2004).
- [54] A. Sykes, *Physics of spherical tokamaks*. Technical Physics, **44**, 1047 (1999).
- [55] R. Akers *et al.*, *Transport and confinement in the mega ampere spherical tokamak (MAST) plasma*, Plasma Physics and controlled Fusion **45**, A175 (2003).
- [56] G.F. Counsell *et al.*, *Overview of MAST results*, Nuclear Fusion **45**, S157-S167 (2005).
- [57] B. Lloyd *et al.*, *Overview of recent experimental results on MAST*, Nucl. Fusion **43**, 1665–1673(2003).
- [58] Y-K. M. Peng *Spherical torus pathway to fusion power*, J. Fusion Energy **17**, 45-59 (1998).
- [59] A. W. Morris *et al.*, *The role of the spherical tokamak in clarifying tokamak physics*, Plasma Physics and Controlled Fusion **41**, B191-B207 (1999).
- [60] A. Sykes *et al.*, *First results from the START tokamak*, Nuclear Fusion **32**, 694-699 (1992).
- [61] A. Sykes *et al.*, *First results from MAST*, Nuclear Fusion **41**, 1423-1433 (2001).
- [62] M. Ono *et al.*, *Overview of the Initial NSTX experimental results*, Nuclear Fusion **41**, 1435-1447 (2001).

- [63] M. Valovic, M. Edwards, D. Gates, S. J. Fielding, T. C. Hender, J. Hugil, A. W. Morris, and the COMPASS team. *L-H transitions and ELMs on COMPASS-D*. In 21st European Physical Society Conference on Controlled Fusion and Plasma Physics, volume **1**, 105-127 (1994). Contributed papers.
- [64] H. R. Wilson and S. C. Cowley, *Theory for explosive ideal magnetohydrodynamic instabilities in plasmas*, Phys Rev Lett **92**, 175006 (2004).
- [65] H. R. Wilson, S. C. Cowley, A. Kirk and P. B. Snyder, *Magnetohydrodynamic stability of the H-mode transport barrier as a model for edge localized modes: an overview**, Plasma Physics and Controlled Fusion **48**, A71-A84 (2006).
- [66] J. P. Freidberg, *Ideal Magnetohydrodynamics*, (Plenum Press, New York, 1987).
- [67] S.I. Braginskii. *Transport processes in a plasma*. In M.A. Leontovich, editor, Reviews of Plasma Physics, page 205. Consultants Bureau, New York, (1965).
- [68] N. Rogers and J. F. Drake, *Diamagnetic stabilization of ideal ballooning modes in the edge pedestal*, Phys. Plasmas **6**, 2797 (1999).
- [69] R. J. Hastie, P. J. Catto, and J. J. Ramos, *Effect of strong radial variation of the ion diamagnetic frequency on internal ballooning modes*, Phys. Plasmas **7**, 4561 (2000).
- [70] A. B. Mikhailovskii, *Instabilities in a confined plasma* (IOP, Bristol, 1998).
- [71] R. D. Hazeltine, and J. D. Meiss, *Plasma Confinement*, (Dover publication, USA, 2003).
- [72] Z. Chang and J.D. Callen, *Generalized gyroviscous force and its effect on the momentum balance equation*, Phys. Fluid B **4**(7), 1766 (1992).
- [73] B. H. Fong, S. C. Cowley, and O. A. Hurricane. *Metastability in magnetically confined plasmas*. Phys. Rev. Lett. **82**, 4651 (1999).
- [74] S. C. Cowley, and M. Artun. *Explosive instabilities and detonation in magnetohydrodynamics*, Phys. Rep. **283**, 185 (1997).

- [75] J. W. Connor, R. J. Hastie, and J. B. Taylor, *High mode number stability of an axisymmetric toroidal plasma*, Proc. R. Soc. Lond. Ser. **365**, 1-17 (1979).
- [76] V. D. Shafranov, *On magnetohydrodynamical equilibrium configurations*, Soviet Physics, JETP, **6**, 545 (1958).
- [77] T. Sato and T. Hayashi, *Externally Driven Magnetic Reconnection and Powerful Magnetic Energy Converter*, Phys. Fluids **22**, 1189-1202 (1979).
- [78] N. Mizuguchi, T. Hayashi, and T. Sato, *Dynamics of spherical tokamak plasma on internal reconnection event*, Phys. Plasmas, **7**, 940-949 (2000).
- [79] N. Mizuguchi, T. Hayashi, and T. Sato, *Nonlinear simulation of Internal Reconnection Event (IRE) in spherical tokamak (in Japanese)*, J. Plasma and Fusion Res., **75**(5) CD-ROM (1999)
- [80] T. Hayashi, N. Mizuguchi, T. H. Watanabe, Y. Todo, T. Sato, and The Complexity Simulation Group, *Nonlinear simulation of Internal Reconnection Event in Spherical Tokamak*, Nuclear Fusion , **40**(3), 721-726 (2000).
- [81] A. Kirk *et al.*, *Evolution of filament structures during Edge-Localized Modes in the MAST Tokamak* **92**, 2185001 (2006).
- [82] W.A. Cooper, *Ballooning instabilities in tokamaks with sheared toroidal flows*, Plasma Phys. Control Fusion **30**, 1805 (1988)
- [83] W. M. Tang, R. L. Dewar and J. Manickam, Nucl. Fusion **22**, 1079 (1982)
- [84] R. Khan, N. Mizuguchi, N. Nakajima, and T. Hayashi *Dynamics of ballooning modes and the relation to Edge Localized Mode in a spherical tokamak*, (submitted to Physics of Plasmas).
- [85] R. Khan, N. Mizuguchi, and T. Hayashi. *Simulation of edge localized modes in spherical tokamak: Effects of ion diamagnetic drift*, (Accepted in Journal of Plasma Physics).
- [86] R. Khan, N. Mizuguchi, and T. Hayashi. *Nonlinear simulation of edge localized mode in spherical tokamak (in Japanese)*, The papers of technical Meeting on Plasma Science and Technology, IEEJ, PST-**05**-65 (2005).
- [87] N. Mizuguchi, R. Khan, and T. Hayashi. *Nonlinear simulation of edge localized mode in ST*, IEEJ Trans. **125**(11) 934 (2005).